

## RESEARCH ARTICLE

10.1002/2016JA023393

## Key Points:

- A 2-D global inductive-dynamic ionosphere/thermosphere model is developed
- Simulation study shows dynamic propagation of the electric field and field-aligned currents and formation of the Pedersen currents
- It is shown that during dynamic stage, the M-I coupling is via the Alfvén waves instead of field-aligned currents or electric field mapping

## Correspondence to:

J. Tu,  
Jiannan\_Tu@uml.edu

## Citation:

Tu, J., and P. Song (2016), A two-dimensional global simulation study of inductive-dynamic magnetosphere-ionosphere coupling, *J. Geophys. Res. Space Physics*, 121, 11,861–11,881, doi:10.1002/2016JA023393.

Received 25 AUG 2016

Accepted 17 NOV 2016

Accepted article online 22 NOV 2016

Published online 20 DEC 2016

## A two-dimensional global simulation study of inductive-dynamic magnetosphere-ionosphere coupling

Jiannan Tu<sup>1</sup> and Paul Song<sup>1</sup>

<sup>1</sup>University of Massachusetts, Laboratory of Space Science and Physics Department, Lowell, Massachusetts, USA

**Abstract** We present the numerical methods and results of a global two-dimensional multifluid-collisional-Hall magnetohydrodynamic (MHD) simulation model of the ionosphere-thermosphere system, an extension of our one-dimensional three-fluid MHD model. The model solves, self-consistently, Maxwell's equations, continuity, momentum, and energy equations for multiple ion and neutral species incorporating photochemistry, collisions among the electron, ion and neutral species, and various heating sources in the energy equations. The inductive-dynamic approach (solving self-consistently Faraday's law and retaining inertia terms in the plasma momentum equations) used in the model retains all possible MHD waves, thus providing faithful physical explanation (not merely description) of the magnetosphere-ionosphere/thermosphere (M-IT) coupling. In the present study, we simulate the dawn-dusk cross-polar cap dynamic responses of the ionosphere to imposed magnetospheric convection. It is shown that the convection velocity at the top boundary launches velocity, magnetic, and electric perturbations propagating with the Alfvén speed toward the bottom of the ionosphere. Within the system, the waves experience reflection, penetration, and rereflection because of the inhomogeneity of the plasma conditions. The reflection of the Alfvén waves may cause overshoot (stronger than the imposed magnetospheric convection) of the plasma velocity in some regions. The simulation demonstrates dynamic propagation of the field-aligned currents and ionospheric electric field carried by the Alfvén waves, as well as formation of closure horizontal currents (Pedersen currents in the *E* region), indicating that in the dynamic stage the M-I coupling is via the Alfvén waves instead of field-aligned currents or electric field mapping as described in convective M-I coupling models.

### 1. Introduction

Magnetosphere and ionosphere-thermosphere are coupled by energy, momentum, and mass exchange. During periods of southward interplanetary magnetic field (IMF) the solar wind and magnetospheric convection drives a two-cell ionospheric convection in the high latitude, while more complicated ionospheric convection patterns occur if the IMF directs to the north. Often, magnetic field-aligned current sheets, namely regions 1 and 2, are formed in the regions of the velocity shear (or reversal). The field-aligned currents or electric potential mapping from the magnetosphere have long been used to represent the electrodynamic coupling between the magnetosphere and ionosphere [e.g., Vasyliūnas, 1970, Wolf, 1970; Richmond, 1995]. While this **E, J** paradigm has been successful in describing electrostatic ( $\nabla \times \mathbf{E} = 0$ ) and quasi steady state ( $\partial/\partial t = 0$ ) magnetosphere-ionosphere (M-I) coupling, it cannot explain the M-I coupling dynamics, in which perturbations of the plasma and neutral flow, and electromagnetic field are coupled in the form of waves, as all wave processes are excluded in the description. In the second edition of his book, Kelley [2009] stated that "Information is transmitted from one region to the other in the solar wind-magnetosphere-ionosphere system by waves of various types." Apparently, electrostatic and quasi steady state method only provides a description of the coupled M-I system, which may not be able to describe the strong oscillations of the ionosphere/thermosphere in response to the changes in the magnetospheric driving forces during important phenomena such as substorms. Indeed, our previous one-dimensional numerical simulations [Song *et al.*, 2009; Tu *et al.*, 2011, 2014] have clearly shown the dynamic processes of the M-I coupling via the MHD waves, particularly the Alfvén waves. Furthermore, Vasyliūnas [2012] has discussed in detail the physical basis of the conventional ionospheric electrodynamic, providing convincing theoretical arguments that applications of the conventional ionospheric electrodynamic are limited to slow time variations and are not applicable to transient processes that are of essential importance in the M-I coupling processes.

Associated with the  $\mathbf{E}, \mathbf{J}$  paradigm, which has mathematical advantages when formulating a steady state system but is nearly impossible to describe a dynamical system [Parker, 2007], it has also long been believed that the primary energy transfer from the magnetosphere and most of energy deposited in the ionosphere-thermosphere occurs in the auroral zone, the region of strong field-aligned current density, even during quiet times without including the energy associated with the particle precipitation. The so-called ionospheric Joule heating, which is essentially the frictional heating *Vasyliūnas and Song* [2005], i.e., caused by the collisions between the ionospheric ions and neutrals, is proportional to  $\nu_{in}\rho(\mathbf{V} - \mathbf{V}_n)^2$ , where  $\nu_{in}$  is the ion-neutral collision frequency,  $\rho$  the plasma mass density, and  $\mathbf{V}$  and  $\mathbf{V}_n$  the plasma and neutral velocity, respectively. Because of the slow response of the neutrals, the disturbances from the magnetosphere appear initially in the plasma velocity and result in velocity differences that produce the heating. Therefore, the heating is primarily dependent on the plasma velocity. In other words, the energy deposit in the ionosphere should occur in regions of high plasma velocity instead of the region of the velocity reversal which corresponds to the region of the field-aligned currents and, in general, smaller speeds. In addition, the region of the energy deposit should also coincide with the region of the energy transfer because the Poynting flux of the Alfvén waves is proportional to  $V_A\rho V^2$ , where  $V_A$  is the Alfvén speed, on the magnetohydrodynamic (MHD) time and spatial scales for the problems of interest. Greater Poynting fluxes have been often observed in the polar cap region and less in the field-aligned region especially during quiet time [Huang *et al.*, 2014].

In this study we investigate the dynamic M-I coupling across the dawn-dusk high-latitude ionosphere using a newly developed two-dimensional self-consistent inductive-dynamic ionosphere-thermosphere model. Here we should clarify that the “wave” discussed in our theory does not need to be sinusoidal oscillations. It refers to any spatially propagating variations because, in principle, they are the summation of a series of sinusoidal waves. On MHD time and spatial scales the coupling between the magnetosphere and ionosphere, as well as among different regions of the ionosphere, is through either Alfvén waves or compressional waves. Therefore, the time-dependent plasma and neutral continuity, momentum, and energy equations, together with Maxwell’s equations, and with collisional and photochemical processes, have to be self-consistently solved. Otherwise, using electrostatic electric field  $\nabla \times \mathbf{E} = 0$  would exclude all the MHD waves and, hence, dynamics of the M-I coupling.

The inductive effects have been used in studying the ionosphere dynamics and the role of Alfvén waves in the dynamics of the field-aligned current. For instance, time-dependent phenomena have been treated as waves using Fourier analysis [Hughes, 1974]. In this approach propagation and reflection effects within the ionosphere are retained, but explicit description of the plasma and neutral dynamics is not incorporated. In the study of *Streltsov and Lotko* [2008], inductive effects of the parallel electric field are included, but neither the energy equations (so that energy exchange between waves and plasma, such as wave heating, is absent) nor the neutral dynamics is solved. In a series of modeling studies, *Birk and Otto* [1996], *Zhu *et al.** [2001], and *Otto *et al.** [2003] incorporated both plasma and neutral dynamics/thermal dynamics; nevertheless, they interpreted the simulation results still in the context of the quasi steady state assumption, or  $\mathbf{E}, \mathbf{J}$  paradigm. The models of *Lysak and Dum* [1983], *Lysak* [2004], *Woodroffe and Lysak* [2012], and *Lysak *et al.** [2013] include the inductive effects and have been used to simulate ULF wave propagation in the structured ionosphere. The ionosphere was, nevertheless, not self-consistently modeled but prescribed by parallel, Pedersen and Hall conductivities.

Our inductive-dynamic approach in modeling the ionosphere-thermosphere differs from previous studies in that we retain inductive effects, dynamics and thermal dynamics of both plasma, and neutrals in the self-consistently evolving structured ionosphere/thermosphere. In our previous simulation studies, we have explored the transient responses of the ionosphere-thermosphere to the imposed magnetospheric convection in one-dimensional geometry [Song *et al.*, 2009; Tu *et al.*, 2011, 2014], which led to the appreciation of the importance of the wave reflection from the low-altitude ionosphere in causing the overshoots and oscillations of the ionosphere perturbations. In addition, the inductive-dynamic simulation with plasma-neutral interaction incorporated has been used to investigate Alfvén wave propagation and reflection in the Sun’s chromosphere as well as heating of the chromosphere by Alfvén wave dissipation through plasma-neutral collisions [Tu and Song, 2013]. In the present study we extend our previous simulations to 2-D geometry and multiple ion and neutral fluids. In the next section we describe the simulation model used in the present simulation, including discussion of governing equations, the implicit numerical scheme, boundary/initial conditions, methods of treating numerical instabilities, stiffness of the equations, and the issue of keeping the magnetic field divergence free. We present simulation results in section 3, and the summary with discussion in section 4.

## 2. Simulation Model

### 2.1. Model Formulation

We use five-moment transport equations for multifluid ( $l$  ion species,  $m$  neutral species, and electrons  $e$ ) in a rotating frame [Schunk and Nagy, 2000], with inclusion of the heat flow terms in energy equations. The continuity, momentum, and energy equations for species  $s$ , in a frame of reference rotating with the Earth, are

$$\frac{\partial \rho_s}{\partial t} + \nabla \cdot (\rho_s \mathbf{v}_s) = \sum_{t \neq s}^{l,m,e} (P_{st} m_t - L_{st} \rho_s) \quad (1)$$

$$\begin{aligned} \frac{\partial \rho_s \mathbf{v}_s}{\partial t} + \nabla \cdot (\rho_s \mathbf{v}_s \mathbf{v}_s) + \nabla p_s = n_s e_s (\mathbf{E} + \mathbf{v}_s \times \mathbf{B}) + \rho_s \mathbf{g} - \rho_s [2\boldsymbol{\Omega} \times \mathbf{v}_s + \boldsymbol{\Omega} \times (\boldsymbol{\Omega} \times \mathbf{r})] \\ - \rho_s \sum_{t \neq s}^{l,m,e} \nu_{st} (\mathbf{v}_s - \mathbf{v}_t) + \sum_{t \neq s}^{l,m,e} (P_{st} m_t \mathbf{v}_t - L_{st} \rho_s \mathbf{v}_s) \end{aligned} \quad (2)$$

$$\begin{aligned} \frac{3}{2} n_s \left[ \frac{\partial k_b T_s}{\partial t} + \nabla \cdot (k_b T_s \mathbf{v}_s) \right] - \frac{1}{2} n_s k_b T_s (\nabla \cdot \mathbf{v}_s) + \nabla \cdot \mathbf{q}_s = \\ \sum_{t \neq s}^{l,m,e} \frac{n_s m_s \nu_{st}}{m_s + m_t} \left[ 3k_b (T_t - T_s) + m_t (\mathbf{v}_t - \mathbf{v}_s)^2 \right] + Q_s - C_s \end{aligned} \quad (3)$$

where  $n_s$ ,  $e_s$ ,  $m_s$ ,  $\mathbf{v}_s$ ,  $T_s$ ,  $p_s$ , and  $\mathbf{q}_s$  are the number density, charge ( $=e$  for ions,  $=-e$  for electrons, and  $=0$  for neutrals, where  $e$  is the elementary charge), mass, bulk velocity, temperature, pressure ( $p_s = n_s k_b T_s$ ,  $k_b$  the Boltzmann constant), and heat flux, respectively, of species  $s$ ;  $\rho_s = n_s m_s$  is the mass density;  $\mathbf{v}_t$  and  $T_t$  are the bulk velocity and temperature, respectively, of species  $t$ ;  $P_{st}$  and  $L_{st}$  are the production rate and loss coefficient of species  $s$  due to photoionization of neutral species  $t$  (for ion species  $s$ ) or chemical reaction with species  $t$ ;  $Q_s$  and  $C_s$  are the heating and cooling rate, respectively; and  $\mathbf{g}$  and  $\boldsymbol{\Omega}$  are the Earth's gravitational acceleration, angular frequency of the Earth rotation, respectively. We have assumed that all ions are singly charged and pressures are isotropic. Note that the terms associated with the species production and loss in the energy equation have been included in heating and cooling terms  $Q_s$  and  $C_s$ .

The electron density can be determined by the quasi-charge neutrality approximation, i.e.,  $n_e \approx \sum_s^l n_s$ . In time scales much longer than the electron plasma and gyro periods, the electron momentum equation may be simplified, leading to the expression for the electric field

$$\mathbf{E} = -\mathbf{v}_e \times \mathbf{B} - \frac{1}{en_e} \nabla p_e - \frac{m_e}{e} \sum_t^{l,m} \nu_{et} (\mathbf{v}_e - \mathbf{v}_t) \quad (4)$$

where  $p_e$  and  $\mathbf{v}_e$  are the electron pressure and bulk velocity, respectively, and  $\nu_{et}$  is the frequencies of electron collision with the other species. The electron pressure is assumed to be isotropic and  $p_e = k_b n_e T_e$ , where  $T_e$  is the electron temperature.

The equation system also includes Maxwell's equations, with assumption of displacement current being negligibly small

$$\frac{\partial \mathbf{B}}{\partial t} = -\nabla \times \mathbf{E} \quad (5)$$

$$\nabla \times \mathbf{B} = \mu_0 \mathbf{J} = \mu_0 e \left( \sum_s^l n_s \mathbf{v}_s - n_e \mathbf{v}_e \right) \quad (6)$$

where  $\mu_0$  is permeability in vacuum. By inserting (4) into (2) and further replacing  $\mathbf{v}_e$  with that calculated from (6) we may rewrite the momentum equation for ion species  $s$  as

$$\begin{aligned} \frac{\partial \rho_s \mathbf{v}_s}{\partial t} + \nabla \cdot (\rho_s \mathbf{v}_s \mathbf{v}_s) + \nabla k_b n_s T_s = n_s e_s \left( \mathbf{v}_s - \frac{1}{n_e} \sum_t^l n_t \mathbf{v}_t \right) \times \mathbf{B} + \frac{n_s}{n_e \mu_0} (\nabla \times \delta \mathbf{B}) \times \mathbf{B} - \frac{n_s}{n_e} \nabla k_b n_e T_e \\ - n_s m_e \sum_t^{l,m} \nu_{et} (\mathbf{v}_e - \mathbf{v}_t) + \rho_s \mathbf{g} - \rho_s [2\boldsymbol{\Omega} \times \mathbf{v}_s + \boldsymbol{\Omega} \times (\boldsymbol{\Omega} \times \mathbf{r})] \\ - \rho_s \sum_{t \neq s}^{l,m,e} \nu_{st} (\mathbf{v}_s - \mathbf{v}_t) + \sum_{t \neq s}^{l,m,e} (P_{st} \mathbf{v}_t m_t - L_{st} \rho_s \mathbf{v}_s) \end{aligned} \quad (7)$$

In the above equation we have assumed that the magnetic field consists of a background field  $\mathbf{B}_0$ , which is assumed to be a dipole magnetic field, current-free and constant in time, and a perturbation field  $\delta\mathbf{B}$ ;  $\mathbf{B} = \mathbf{B}_0 + \delta\mathbf{B}$ . Finally, substituting (4) into (5), we reach

$$\frac{\partial \delta \mathbf{B}}{\partial t} = \nabla \times (\mathbf{v}_e \times \mathbf{B}) - \frac{k_b}{en_e} \nabla n_e \times \nabla T_e + \frac{m_e}{e} \sum_t^{l,m} \nabla \times v_{et} (\mathbf{v}_e - \mathbf{v}_t) \quad (8)$$

The equations (1), (3), (7), and (8) form a set of multifluid-collisional-Hall MHD equations, including the neutral dynamics. Note that the neutral momentum equations have a similar form of (7) but without the first four terms, involving the magnetic field and electrons, on the right-hand side. These equations are normalized based on four basic normalization constants: length  $r_0 = R_E = 6371.2 \times 10^3$  m, number density  $n_0 = 10^{10} \text{ m}^{-3}$ , proton mass  $m_p = 1.6702 \times 10^{-27}$  kg, and equatorial magnetic field induction on the Earth's surface at the equator  $B_{\text{eq}} = 3.12 \times 10^{-5}$  Tesla. Other normalization constants for the remaining quantities can be derived by the combination of these four parameters. The only differences between normalized and unnormalized equations are that  $k_b$  and  $\mu_0$  are removed from the normalized equations and  $m_e/e$  in (8) is replaced with  $1/\bar{\Omega}_e$ , where  $\bar{\Omega}_e$  is normalized electron gyrofrequency calculated with  $B_0$ :  $\bar{\Omega}_e = (eB_0/m_e) t_0$ . The normalization constant for time  $t_0 = r_0/v_0$  with  $v_0 = B_0/(\mu_0 n_0 m_p)^{1/2}$ .

The final form of multifluid-collisional-Hall MHD equations solved in our simulation model may be concisely written, after normalization, as

$$\frac{\partial \bar{\mathbf{U}}}{\partial \bar{t}} + \bar{\nabla} \cdot \bar{\mathbf{F}} = \bar{\mathbf{R}}(\bar{\mathbf{U}}) \quad (9)$$

$$\frac{\partial \delta \bar{\mathbf{B}}}{\partial \bar{t}} - \bar{\nabla} \times (\bar{\mathbf{v}}_e \times \bar{\mathbf{B}}) = \bar{\mathbf{R}}(\delta \bar{\mathbf{B}}) \quad (10)$$

where  $\bar{\mathbf{v}}_e = \left( \sum_s^l \bar{n}_s \bar{\mathbf{v}}_s \right) / \bar{n}_e - \bar{\nabla} \times \delta \bar{\mathbf{B}} / \bar{e} \bar{n}_e$ , and

$$\bar{\mathbf{U}} = \begin{pmatrix} \bar{\rho}_s \\ \bar{\rho}_s \bar{\mathbf{v}}_s \\ \bar{T}_s \\ \bar{T}_e \end{pmatrix}, \quad \bar{\mathbf{F}} = \begin{pmatrix} \bar{\rho}_s \bar{\mathbf{v}}_s \\ \bar{\rho}_s \bar{\mathbf{v}}_s \bar{\mathbf{v}}_s \\ \bar{T}_s \bar{\mathbf{v}}_s \\ \bar{T}_e \bar{\mathbf{v}}_e \end{pmatrix}$$

Specific expressions for the components of  $\bar{\mathbf{R}}(\bar{\mathbf{U}})$  are given by (note that the first four terms of the right-hand side of (12) vanish for neutral species)

$$\bar{R}(\bar{\rho}_s) = \sum_{t \neq s}^{l,m,e} (\bar{P}_{st} \bar{m}_t - \bar{L}_{st} \bar{\rho}_s) \quad (11)$$

$$\begin{aligned} \bar{R}(\bar{\rho}_s \bar{\mathbf{v}}_s) &= \bar{e} \bar{n}_s \left( \bar{\mathbf{v}}_s - \frac{1}{\bar{n}_e} \sum_t^l \bar{n}_t \bar{\mathbf{v}}_t \right) \times \bar{\mathbf{B}} + \frac{\bar{n}_s}{\bar{n}_e} (\bar{\nabla} \times \delta \bar{\mathbf{B}}) \times \bar{\mathbf{B}} - \frac{\bar{n}_s}{\bar{n}_e} \bar{\nabla} \bar{n}_e \bar{T}_e \\ &\quad - \bar{n}_s \bar{m}_e \sum_{t \neq s}^{l,m} \bar{v}_{et} (\bar{\mathbf{v}}_e - \bar{\mathbf{v}}_t) - \bar{\rho}_s \sum_{t \neq s}^{l,m,e} \bar{v}_{st} (\bar{\mathbf{v}}_s - \bar{\mathbf{v}}_t) - \bar{\nabla} \bar{n}_s \bar{T}_s \\ &\quad - \bar{\rho}_s [2\bar{\Omega} \times \bar{\mathbf{v}}_s + \bar{\Omega} \times (\bar{\Omega} \times \bar{\mathbf{r}})] + \bar{\rho}_s \bar{\mathbf{g}} + \sum_{t \neq s}^{l,m,e} (\bar{P}_{st} \bar{\mathbf{v}}_t \bar{m}_t - \bar{L}_{st} \bar{\rho}_s \bar{\mathbf{v}}_s) \end{aligned} \quad (12)$$

$$\bar{R}(\bar{T}_s) = \frac{1}{3} \bar{T}_s (\bar{\nabla} \cdot \bar{\mathbf{v}}_s) - \frac{2}{3 \bar{n}_s} \bar{\nabla} \cdot \bar{\mathbf{q}}_s + \sum_{t \neq s}^{l,m,e} \frac{\bar{m}_s \bar{v}_{st}}{\bar{m}_s + \bar{m}_t} \left[ 2(\bar{T}_t - \bar{T}_s) + \frac{2}{3} \bar{m}_t (\bar{\mathbf{v}}_t - \bar{\mathbf{v}}_s)^2 \right] + \frac{2}{3 \bar{n}_s} (\bar{Q}_s - \bar{C}_s) \quad (13)$$

$$\bar{R}(\bar{T}_e) = \frac{1}{3} \bar{T}_e (\bar{\nabla} \cdot \bar{\mathbf{v}}_e) - \frac{2}{3 \bar{n}_e} \bar{\nabla} \cdot \bar{\mathbf{q}}_e + \sum_{t \neq s}^{l,m} \frac{\bar{m}_e \bar{v}_{st}}{\bar{m}_e + \bar{m}_t} \left[ 2(\bar{T}_t - \bar{T}_e) + \frac{2}{3} \bar{m}_t (\bar{\mathbf{v}}_t - \bar{\mathbf{v}}_e)^2 \right] + \frac{2}{3 \bar{n}_e} (\bar{Q}_e - \bar{C}_e) \quad (14)$$

$$\bar{\mathbf{R}}(\delta \bar{\mathbf{B}}) = -\frac{1}{\bar{e} \bar{n}_e} \bar{\nabla} \bar{n}_e \times \bar{\nabla} \bar{T}_e + \frac{1}{\bar{\Omega}_e} \sum_t^{l,m} \bar{\nabla} \times \bar{v}_{et} (\bar{\mathbf{v}}_e - \bar{\mathbf{v}}_t) \quad (15)$$

In the above equations variables with a bar are normalized. Note that the normalized magnetic induction equation (10) is written in a nonconserved form in order to have the divergence-free perturbation magnetic field automatically satisfied with a staggered grid system, as will be discussed in section 2.5.2.

## 2.2. Photoionization and Chemical Reactions

We consider five ion species ( $O^+$ ,  $H^+$ ,  $O_2^+$ ,  $N_2^+$ , and  $NO^+$ ), and six neutral species (O, H,  $O_2$ ,  $N_2$ , NO, and N) in the present model. The  $N_2$  and N are included in order to calculate the production of  $NO^+$  ions through the chemical reactions of these neutral particles with  $O_2^+$  ions. The production rate  $P_{st}$  and the loss coefficient  $L_{st}$  in (1) and (2) are determined by production and loss processes of the species. Ions are produced by photoionization of neutrals. One ion species may be produced by chemical reactions of another ion species with neutrals. Meanwhile, the ions participating in the reactions are lost; production and loss of individual neutral species are also through such chemical reactions.

The dayside photoionization rate of neutral species  $s$  is given by [e.g., Schunk and Nagy, 2000]

$$P_s(z) = n_s(z) \sum_{\lambda} \sigma_s^i(\lambda) F(\lambda) \exp \left[ - \sum_t \sigma_t^a(\lambda) \int_z^{\infty} n_t(l) dl \right] \quad (16)$$

where  $n_s$  and  $n_t$  are the densities of neutral species  $s$  and  $t$ , respectively,  $F(\lambda)$  is the incident solar EUV flux at wavelength  $\lambda$ ,  $\sigma_s^i(\lambda)$  and  $\sigma_t^a(\lambda)$  are the ionization and photoabsorption cross sections, respectively, of species  $s$  and  $t$  at  $\lambda$ . The integral  $\int_z^{\infty} n_t(l) dl$  is evaluated along a ray from the Sun to the point of interest at altitude  $z$ . We use the method developed by Smith and Smith [1972] for dayside photoionization. The incident solar EUV flux is calculated from the EUVAC model developed by Richards *et al.* [1994], which is based on a reference flux  $F_{74113}$  in 37 bins of the wavelength

$$F(\lambda_i) = F_{74113} \{ 1 + A_i [(F_{107} + F_{107A})/2 - 80] \}, \quad i = 1, 2, \dots, 37 \quad (17)$$

where  $F_{107}$  is 10.7 cm solar flux and  $F_{107A}$  is its 81 day average (centered at the date of  $F_{107}$ ). The values of  $F_{74113}$  and  $A_i$  for 37 wavelength bins from 50 to 1050 Å, along with the photoabsorption and photoionization cross sections in the 37 bins for various neutral species, are given in Richards *et al.* [1994]. In our simulations we calculate photoionization rates for O,  $O_2$ , and  $N_2$  from (16). The initial densities and temperatures of O,  $O_2$ ,  $N_2$ , H, and N are determined by the empirical thermospheric model NRLMSISE00 [Picone *et al.*, 2002]. NRLMSISE00 does not provide the NO density so that the initial NO density is calculated using the formula of Mitra [1968]. The subsequent evolution of the densities and temperatures of all the neutral species are solved using their continuity, momentum, and temperature equations.

The same method of Strobel *et al.* [1980] is used to calculate the nighttime photoionization due to starlight (stellar continuum radiation in the spectral interval 911–1026 Å) and resonance scattering of solar  $Ly-\alpha$  and  $Ly-\beta$  into the night sector. Such nighttime photoionization is important to maintain the nighttime  $E$  region of the ionosphere.

Charge exchange and dissociative reactions are also important processes that can change ion species from one to another so that the mass densities for both involved species change accordingly. We consider 21 reactions, listed in Huba *et al.* [2000]. Four major recombination processes, namely,  $O^+ + e \rightarrow O$ ,  $H^+ + e \rightarrow H$ ,  $NO^+ + e \rightarrow NO$ , and  $O_2^+ + e \rightarrow O_2$ , are considered in the present study to account the loss of an ion-electron pair. The reaction rates of these recombination reactions can be obtained from Schunk and Nagy [2000].

## 2.3. Collision Frequencies

The collisional terms in the governing equations include interspecies collisions between electrons and ions, electrons and neutrals, between different ion species, ions and neutrals, and between different neutral species. The collision frequencies for the electron-ion, electron-neutral, and ion-neutral are taken from Schunk and Nagy [2000] and are not repeated here. The neutral-electron and neutral-ion collision frequencies can be evaluated by using momentum conservation during the interspecies collisions, for example,  $\rho_{O^+} \nu_{O^+,O_2} = \rho_{O_2} \nu_{O_2,O^+}$ , where  $\rho_{O^+}$  and  $\rho_{O_2}$  are  $O^+$  and  $O_2$  mass densities, respectively, and  $\nu_{O^+,O_2}$  and  $\nu_{O_2,O^+}$  are the collision frequencies between  $O^+$  and  $O_2$ , and between  $O_2$  and  $O^+$ , respectively.

The collision frequencies of a molecule of type  $s$  with molecules of type  $t$  may be written as [Chapman and Cowling, 1970]

$$v_{st} = \frac{n_s m_s + n_t m_t}{m_s m_t (n_s + n_t)} \frac{k_b T_{st}}{D_{st}} \quad (18)$$

where  $T_{st} = (m_s T_t + m_t T_s) / (m_s + m_t)$  is the reduced temperature, and  $D_{st}$  is the binary diffusion coefficient. The binary diffusion coefficient can be expressed as, for the hard sphere interactions between neutral species  $s$  and  $t$ ,  $D_{st} = CT_{st}^\alpha / (n_s + n_t)$ , where  $C$  and  $\alpha$  are two constants with values depending on the pairs of species. For the neutral species considered,  $D_{st}$  are given in  $\text{cm}^2 \text{s}^{-1}$  for temperature range of 250–2000 K [Banks and Kockarts, 1973]

$$D_{\text{O},\text{O}_2} = 9.69 \times 10^{14} \frac{T_{\text{O},\text{O}_2}^{0.774}}{n_{\text{O}} + n_{\text{O}_2}} \quad (19)$$

$$D_{\text{O},\text{N}_2} = 9.69 \times 10^{14} \frac{T_{\text{O},\text{N}_2}^{0.774}}{n_{\text{O}} + n_{\text{N}_2}} \quad (20)$$

$$D_{\text{O}_2,\text{N}_2} = 7.15 \times 10^{14} \frac{T_{\text{O}_2,\text{N}_2}^{0.75}}{n_{\text{O}_2} + n_{\text{N}_2}} \quad (21)$$

$$D_{\text{H},\text{O}} = 5.70 \times 10^{15} \frac{T_{\text{H},\text{O}}^{0.708}}{n_{\text{H}} + n_{\text{O}}} \quad (22)$$

$$D_{\text{H},\text{O}_2} = 4.75 \times 10^{15} \frac{T_{\text{H},\text{O}_2}^{0.711}}{n_{\text{H}} + n_{\text{O}_2}} \quad (23)$$

$$D_{\text{H},\text{N}_2} = 4.87 \times 10^{15} \frac{T_{\text{H},\text{N}_2}^{0.698}}{n_{\text{H}} + n_{\text{N}_2}} \quad (24)$$

where diffusion coefficient  $D_{\text{O}_2,\text{N}_2}$  is taken from Colegrove [1966] evaluated with  $P_0=10^6 \text{ dyn cm}^{-2}$  and  $T_0=273 \text{ K}$  [Dickinson and Ridley, 1972] being inserted. It should be noted that strictly speaking, the binary diffusion coefficients are defined with the assumption that two species have the same temperature. In this study we take  $T_{st}$  as the common temperature for the binary diffusion coefficients. Using above binary diffusion coefficients in (18), we may obtain

$$v_{\text{O},\text{O}_2} = 2.66216 \times 10^{-11} (n_{\text{O}} + 2n_{\text{O}_2}) T_{\text{O},\text{O}_2}^{0.226} \quad (25)$$

$$v_{\text{O},\text{N}_2} = 7.60616 \times 10^{-12} (4n_{\text{O}} + 7n_{\text{N}_2}) T_{\text{O},\text{N}_2}^{0.226} \quad (26)$$

$$v_{\text{O}_2,\text{N}_2} = 5.15410 \times 10^{-12} (8n_{\text{O}_2} + 7n_{\text{N}_2}) T_{\text{O}_2,\text{N}_2}^{0.25} \quad (27)$$

$$v_{\text{H},\text{O}} = 9.05133 \times 10^{-12} (n_{\text{H}} + 16n_{\text{O}}) T_{\text{H},\text{O}}^{0.292} \quad (28)$$

$$v_{\text{H},\text{O}_2} = 5.43880 \times 10^{-12} (n_{\text{H}} + 32n_{\text{O}_2}) T_{\text{H},\text{O}_2}^{0.289} \quad (29)$$

$$v_{\text{H},\text{N}_2} = 6.05369 \times 10^{-12} (n_{\text{H}} + 28n_{\text{N}_2}) T_{\text{H},\text{N}_2}^{0.302} \quad (30)$$

where the collision frequencies have the units of  $\text{s}^{-1}$  and the number densities are in  $\text{cm}^{-3}$ . An issue worth mentioning is that although the above collision frequencies are only valid in the region where collisions occur frequently, i.e., in the lower thermosphere; and they may not be accurate at high altitudes where collisions

are less frequent, the effects of collisions are not important at high altitudes. This is because the above collision frequencies decrease with altitude exponentially with the densities so that the inaccuracy of the collision frequencies will not affect appreciably the numerical results at high altitudes.

#### 2.4. Heating and Cooling Rates

The thermal electron heat source is the photoelectrons produced in the photoionization processes and precipitating electrons in the cusp and auroral oval. In the present study, we do not include the effects of the precipitating electrons. The photoionization heating rate is often calculated using parameterization developed by *Swartz and Nisbet* [1972]. This parameterization was improved by *Smithtro and Solomon* [2008] with the help of physical calculations using GLOW model of photoelectron transport and electron heating [*Solomon et al.*, 1988]. The electron heating rate at low altitudes is thought as local, i.e., by locally produced photoelectrons and newly created thermal electrons. The heating rate is calculated as the sum of two heating rates

$$Q_{\text{photo}} = Q^{0-55\text{nm}} + Q^{55-105\text{nm}}, \quad (31)$$

where  $Q^{0-55\text{nm}}$  and  $Q^{55-105\text{nm}}$  are, respectively, the heating rates due to solar photons of wavelength 0–55 nm and 55–105 nm. The detailed discussion about how to determine these heating rates are given in *Smithtro and Solomon* [2008]

At higher altitudes the electron heating by photoelectrons are primarily determined by the photoelectrons transported from their source regions at lower altitudes. The production of photo electrons at high altitudes is negligible and the heating rate is dependent on the local electron density

$$Q_{\text{photo}} = qn_e \quad (32)$$

where  $q$  is the photoelectron energy per thermal electron (eV). It is calculated by accounting the reduction of photoelectron energy on the transport path along the magnetic field lines, owing to energy transfer to thermal electrons [*Millward et al.*, 1996]

$$q(z) = q_0 \frac{B}{B_0} \exp\left(-\sigma \int_{z_0}^z n_e ds\right) \quad (33)$$

where  $B$  and  $B_0$  are magnetic field strength at altitude  $z$  and transition altitude  $z_0$ , respectively, along the same field line and  $q_0$  is the photoelectron energy per thermal electron at  $z_0$ ,  $\sigma = 7 \times 10^{-14} \text{cm}^2$ , in line with *Smithtro and Solomon* [2008]. The transition altitude  $z_0$  is set at where the neutral pressure  $P_n = 1.5 \mu\text{Pa}$ , corresponding to an altitude of 350–550 km, depending on the level of solar activity [*Smithtro and Solomon*, 2008].

In the lower ionosphere the elastic collisions of electrons with the ions and neutrals, along with inelastic collisions, i.e., rotational and vibrational excitation of the molecular neutrals by the thermal electrons, are the dominant cooling processes for the thermal electron population. The fine structure excitation of atomic oxygen and excitation of nitrogen atoms also play important roles in cooling thermal electrons. The electron cooling due to the elastic collisions with ions and neutrals are treated as heat exchanges with ions and neutrals and already included in the first term on the right-hand side of (3). The electron cooling rates corresponding to the excitation of neutral species have been described by many previous studies and are compiled in *Schunk and Nagy* [2000]. These electron cooling rates are included in the  $C_e$  term of the electron temperature equation.

Major heat sources of the thermosphere include absorption of the solar extreme ultraviolet (EUV, wavelength  $\lambda < 105 \text{ nm}$ ), absorption of Schumann Runge continuum (SRC,  $\lambda = 125 - 152 \text{ nm}$ ) and Schumann Runge bands (SRB,  $\lambda = 152 - 175 \text{ nm}$ ), electron-neutral and ion-neutral collisions, and quenching of excited atomic oxygen  $\text{O}(^1D)$  by  $\text{N}_2$  and  $\text{O}_2$  [*Robel et al.*, 1987]. The heating due to the absorption of the solar EUV radiation is given by *Harris and Priester* [1962]

$$Q_{\text{EUV},s} = \epsilon_s n_s \sum_{\lambda} \sigma_s^a(\lambda) F_{\infty}(\lambda) \frac{hc}{\lambda} \exp\left[-\sum_t \sigma_s^a(\lambda) \int_z^{\infty} n_t(l) dl\right] \quad (34)$$

where  $n_s$  and  $n_t$  are neutral density of species  $s$  and  $t$ , respectively;  $\sigma_s^a(\lambda)$  is the absorption cross section of species  $s$  at the wavelength  $\lambda$ ;  $F_{\infty}(\lambda)$  is the solar EUV flux at  $\lambda$  incident at the top of the atmosphere;  $hc/\lambda$  is

the photon energy with  $h$  the Planck's constant and  $c$  the speed of light; and  $\epsilon_s$  is the heating efficiency for the species  $s$ . The integral inside the bracket is calculated with the same method as that in (16). The heating efficiency  $\epsilon_s$  is a function of altitude, local time, season, and solar cycle, and its peak value is about 50% [Stolarski *et al.*, 1975; Torr *et al.*, 1980].

The thermospheric cooling is primarily caused by the infrared radiative loss due to NO at 5.3  $\mu\text{m}$ , O at 63  $\mu\text{m}$ , and 147  $\mu\text{m}$ , and CO<sub>2</sub> at 15  $\mu\text{m}$ . We only include cooling by the radiative energy loss of NO and O, because above the 80 km the CO<sub>2</sub> is not an important species and is not included in the simulation model, although more cooling effects can be readily added. Bates [1951] studied the rate of energy loss of O radiation assuming an optically thin atmosphere. Later, Kockarts and Peetermans [1970] introduced a masking factor to the cooling rates given by Bates [1951] to compensate the overestimate of the atomic oxygen emissions in the altitude range of 100–150 km owing to the assumption of an optical thin atmosphere. The cooling rates, corresponding to 63 and 147  $\mu\text{m}$  emissions, are then given by

$$C_{\text{O},63\mu\text{m}} = (1 - \chi) \frac{1.69 \times 10^{-18} n(\text{O}) \exp(-228/T_0)}{1 + 0.6 \exp(-228/T_0) + 0.2 \exp(-326/T_0)} \quad (35)$$

$$C_{\text{O},147\mu\text{m}} = (1 - \chi) \frac{4.59 \times 10^{-20} n(\text{O}) \exp(-326/T_0)}{1 + 0.6 \exp(-228/T_0) + 0.2 \exp(-326/T_0)} \quad (36)$$

where the cooling rates are in units of  $\text{ergs cm}^{-3} \text{s}^{-1}$ ,  $T_0$  is the temperature of atomic oxygen O, and  $1 - \chi$  is the reduction factor. The calculation of masking factor  $\chi$  was discussed in detail in Kockarts and Peetermans [1970]. The cooling due to NO emission at 5.3  $\mu\text{m}$  used in the present model is that developed by Kockarts [1980]

$$C_{\text{NO},5.3\mu\text{m}} = \frac{3.24015 \times 10^{-22} n(\text{NO})n(\text{O})}{6.5 \times 10^{-11} n(\text{O}) + 13.3} \exp\left(-\frac{2714.57}{T}\right) \quad (37)$$

with the cooling rate in units of  $\text{ergs cm}^{-3} \text{s}^{-1}$ , density in  $\text{cm}^{-3}$ , and temperature in K. Since the temperature of NO is not calculated, we use the oxygen temperature for the temperature in the above equation;  $T = T_0$ .

## 2.5. Numerical Scheme

### 2.5.1. Difference Method and Grid System

Solving the multifluid-collisional-Hall MHD equations described in the previous sections is a challenging task, requiring special techniques to treat the stiffness and numerical instabilities, which are particularly crucial in the ionosphere where strong interactions take place among disparate fluids through collisions and chemical reactions, as well as coupling through electromagnetic forces. In this section we discuss the numerical algorithm and techniques used in solving the multifluid-collisional-Hall MHD equations in the ionosphere/thermosphere. In the present study we consider a two-dimensional simulation domain: a dawn-dusk magnetic meridian, for which the  $z$  axis of the cylindrical coordinates is toward the Sun from the center of the Earth. The normalized governing equations (9) and (10) are solved in a cylindrical coordinate system  $(\bar{r}, \theta, \bar{z})$ , where  $\theta$  is the azimuthal angle and  $\bar{r} = (\bar{x}^2 + \bar{y}^2)^{1/2}$  is the normalized radial distance, with  $\bar{x}$  and  $\bar{y}$  in the dawn-dusk magnetic meridian. The  $\bar{x}$  axis is from the center of the Earth toward the northern magnetic pole, and the  $\bar{y}$  axis is perpendicular to the  $\bar{x}$  axis. Viewing from the Sun, the azimuthal angle  $\theta$  varies counterclockwise. Figure 1 schematically shows the coordinates and grid system of the simulation domain. All the variables (density, temperature, and three-component velocities of electrons, multiple ion, and neutral species, as well as three-component magnetic field) are assumed to be uniform along the  $\bar{z}$  axis. Therefore the normalized differential operator  $\bar{\nabla}$  is expressed as

$$\bar{\nabla} = \hat{\mathbf{r}} \frac{\partial}{\partial \bar{r}} + \hat{\boldsymbol{\theta}} \frac{\partial}{\partial \theta} \quad (38)$$

To achieve the desired resolution and meanwhile to make the code efficient, nonuniform grids are necessary with finer grids at low altitudes and coarser ones at high altitudes since the scale height is small in the  $E$  region of the ionosphere compared to that at higher altitudes. Nevertheless, to keep a second order of

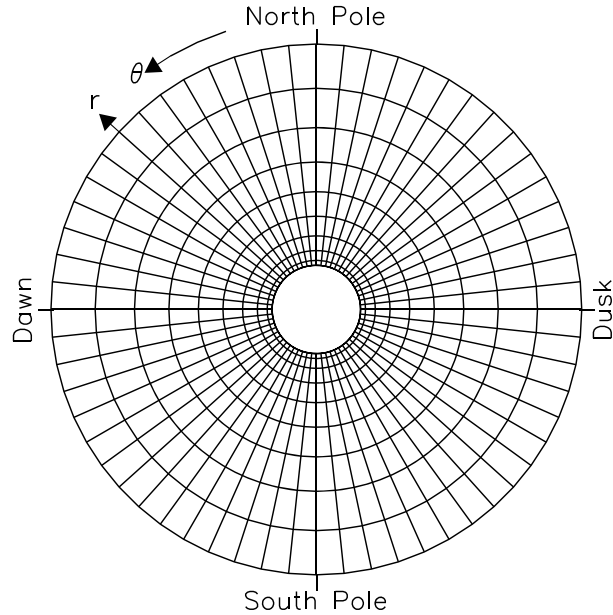


**Figure 1.** Schematic display of the coordinates and grid system of the 2-D simulation domain.

accuracy in space using the nonuniform grids for the difference equations could further complicate an already complicated algorithm. Therefore, the  $\bar{r}$  and  $\theta$  are transformed by using

$$\bar{r} = \bar{r}_b + (\bar{r}_u - \bar{r}_b) \frac{\sinh(x_1/d)}{\sinh(N_1/d)} \quad (39)$$

$$\theta = \frac{2\pi}{N_2} x_2 \quad (40)$$

where  $\bar{r}_b$  and  $\bar{r}_u$  are the normalized radial distance at the lower and upper boundaries of the simulation domain, respectively;  $N_1$  and  $N_2$  are the number of cells along  $\bar{r}$  and  $\theta$  axes, respectively; and  $d$  is a factor for properly stretching the  $\bar{r}$  axis so that there are more cells at low altitudes. From these two expressions we have

$$\bar{\nabla} = \frac{\hat{r}}{h_1} \frac{\partial}{\partial x_1} + \frac{\hat{\theta}}{h_2} \frac{\partial}{\partial x_2} \quad (41)$$

where

$$h_1 = \frac{(\bar{r}_u - \bar{r}_b) \cosh(x_1/d)}{d \sinh(N_1/d)} \quad (42)$$

$$h_2 = \frac{2\pi}{N_2} r \quad (43)$$

It is interesting to note that in the coordinates  $(x_1, x_2)$  the grid cell size is uniform:  $\Delta x_1 = \Delta x_2 = 1$ . The difference representation of partial differential in these coordinates will retain second-order accuracy numerically if a centered difference scheme is used, even though the grid cells are nonuniform in  $\bar{r}$ .

We use a second-order backward difference formula (BDF2) [Curtiss and Hirschfelder, 1952] to represent time derivatives in (9) and (10). The BDF2 scheme expresses a time derivative term with  $\mathbf{U}$  on the  $t + \Delta t$ ,  $t$  and  $t - \Delta t$  time levels, which in the case of a constant time step leads to

$$\frac{3}{2} \frac{\bar{\mathbf{U}}^{t+\Delta t} - \bar{\mathbf{U}}^t}{\Delta \bar{t}} - \frac{1}{2} \frac{\bar{\mathbf{U}}^t - \bar{\mathbf{U}}^{t-\Delta t}}{\Delta \bar{t}} + \bar{\nabla} \cdot \bar{\mathbf{F}}^{t+\Delta t} = \bar{\mathbf{R}}(\bar{\mathbf{U}}^{t+\Delta t}) \quad (44)$$

$$\frac{3}{2} \frac{\delta \bar{\mathbf{B}}^{t+\Delta t} - \delta \bar{\mathbf{B}}^t}{\Delta \bar{t}} - \frac{1}{2} \frac{\delta \bar{\mathbf{B}}^t - \delta \bar{\mathbf{B}}^{t-\Delta t}}{\Delta \bar{t}} - \bar{\nabla} \times [\bar{\mathbf{v}}_i^{t+\Delta t} \times (\bar{\mathbf{B}}_0 + \delta \bar{\mathbf{B}}^{t+\Delta t})] = \bar{\mathbf{R}}(\delta \bar{\mathbf{B}}^{t+\Delta t}) \quad (45)$$

We have used flux  $\bar{\mathbf{F}}$  and  $\bar{\mathbf{U}}$  on the right-hand side at the time step  $t + \Delta t$  so that this is a fully implicit difference scheme, which helps overcome the stiffness caused by collision terms with very large collision frequencies (up to  $10^6$  Hz) and Lorentz force terms  $\nabla \times \delta \mathbf{B} \times \mathbf{B}$ . The vector  $\bar{\mathbf{U}}^{t-\Delta t}$  is not available at the first time step ( $t=0$ ), we simply use a backward Euler scheme to advance  $\bar{\mathbf{U}}$  (and  $\delta \mathbf{B}$ ) from  $t=0$  to  $t = \Delta t$ . Then the BDF2 scheme is used to determine solutions of  $\bar{\mathbf{U}}$  (and  $\delta \mathbf{B}$ ) for the subsequent time steps.

As mentioned previously, the computational domain in the coordinates  $(x_1, x_2)$  is divided as  $N_1 \times N_2$  cells and the grid spacing is  $\Delta x_1 = \Delta x_2 = 1$ . We use a staggered grid system in which all the unknowns except components of the perturbation magnetic field along  $x_1$  and  $x_2$  direction are defined at the cell center  $(i, j)$ , where  $i = 0, 1, 2, \dots, N_1$  and  $j = 0, 1, 2, \dots, N_2$  are grid indexes along  $x_1$  and  $x_2$ , respectively. For the magnetic field components, we define  $\bar{B}_r$  at  $(i, j + 1/2)$ ,  $\bar{B}_\theta$  at  $(i + 1/2, j)$ , and  $\bar{B}_z$  at  $(i + 1/2, j + 1/2)$ . Thereafter, the subscripts  $r, \theta$ , and  $z$  represent radial, azimuthal, and sunward components, respectively, of the velocity or magnetic field (see Figure 1 for definition of the coordinate system). While staggered  $\bar{B}_r$  and  $\bar{B}_\theta$  benefit the divergence-free requirement of the magnetic field, defining  $\bar{B}_z$  at the cell corner  $(i + 1/2, j + 1/2)$  helps avoid unstable solutions caused by the  $\bar{\mathbf{J}} \times \bar{\mathbf{B}}$  term in the ion momentum equations, a situation similar to defining velocity components at the cell faces while the pressure is at the cell center so that the velocity component is staggered with the pressure gradient, which mitigates the checkerboard instability [Sigmund and Petersson, 1998].

We use the centered difference to approximate spatial derivatives so that the spatial difference is of the second order of accuracy. The calculation of the divergence of flux in (9) is treated by a ZIP-type differencing [Hirt, 1968]. For example, the density advection along the  $x_1$  direction is approximated as (the bars over normalized variables have been removed)

$$\frac{1}{h_1} \frac{\partial n_s v_{s,r}}{\partial x_1} \Big|_{ij} \approx \frac{1}{h_{1,j}} \frac{(n_s v_{s,r})_{i+1/2,j} - (n_s v_{s,r})_{i-1/2,j}}{\Delta x_1} \quad (46)$$

The ZIP method conserves the flux by defining the flux at the cell interface as

$$(n_s v_{s,r})_{i+1/2,j} = \frac{1}{2} (n_{s,ij} v_{s,r,i+1,j} + n_{s,i+1,j} v_{s,r,i,j}) \quad (47)$$

Such ZIP-type differencing has the property that introduces no truncation errors which contribute to diffusion of a quantity [Hirt, 1968].

Equations (44) and (45) form a set of nonlinear algebraic equations. We adapt a nonlinear equation solver from the Portable Extensible Toolkit for Scientific Computation (PETSc) software package developed by PETSc team at Argonne National Laboratory. The scalable nonlinear equations solver from the PETSc package is an efficient and extensible tool for solving nonlinear equations using a Newton-like iterative method, which in turn utilizes one of Krylov subspace algorithms [Kelley, 2003] to solve linear equation system at each Newton-like iteration [e.g., Balay et al., 1997].

### 2.5.2. Divergence-Free of the Magnetic Field

A prominent feature of defining  $\bar{B}_r$  and  $\bar{B}_\theta$  at staggered grids is that the divergence-free magnetic field is automatically satisfied. In fact, the time derivative of the magnetic flux over the surfaces of a cell with four grid vertexes  $(i, j)$ ,  $(i + 1, j)$ ,  $(i + 1, j + 1)$ , and  $(i, j + 1)$  is given by

$$\begin{aligned} \frac{\partial}{\partial t} \oint \mathbf{B} \cdot d\mathbf{S} &= \frac{\partial}{\partial t} (h_{2,i+1} B_{r,i+1,j+1/2} - h_{2,i} B_{r,i,j+1/2}) \Delta x_2 \\ &+ \frac{\partial}{\partial t} (B_{\theta,i+1/2,j+1} - B_{\theta,i+1/2,j}) h_{1,i+1/2} \Delta x_1 \end{aligned} \quad (48)$$

From (10) we have in the coordinates  $(x_1, x_2)$  (note  $\Delta x_1 = \Delta x_2 = 1$ )

$$\begin{aligned} \frac{\partial B_{r,i,j+1/2}}{\partial t} &= \frac{1}{h_{2,i}} \left[ (v_{e,r} B_\theta)_{i,j+1} - (v_{e,r} B_\theta)_{i,j} \right] - \frac{1}{h_{2,j}} \left[ (v_{e,\theta} B_r)_{i,j+1} - (v_{e,\theta} B_r)_{i,j} \right] \\ &+ \frac{1}{h_{2,i} \Omega_e} \sum_t^{l,m} \left[ v_{et,i,j+1} (v_{e,z} - v_{t,z})_{i,j+1} - v_{et,i,j} (v_{e,z} - v_{t,z})_{i,j} \right] \end{aligned} \quad (49)$$

$$\begin{aligned} \frac{\partial B_{\theta,ij+1/2j}}{\partial t} = & \frac{1}{h_{1,i+1/2}} \left[ (v_{e,\theta} B_r)_{i+1,j} - (v_{e,\theta} B_r)_{ij} \right] - \frac{1}{h_{1,i+1/2}} \left[ (v_{e,r} B_\theta)_{i+1,j} - (v_{e,r} B_\theta)_{ij} \right] \\ & - \frac{1}{h_{1,i+1/2} \Omega_e} \sum_t^{l,m} \left[ v_{et,i+1,j} (v_{e,z} - v_{t,z})_{i+1,j} - v_{et,ij} (v_{e,z} - v_{t,z})_{ij} \right] \end{aligned} \quad (50)$$

By inserting the above two equations into (48), it is shown that due to perfect cancelation of the terms, we have

$$\frac{\partial}{\partial t} \oint \mathbf{B} \cdot d\mathbf{S} = 0 \quad (51)$$

which implies that if initially the magnetic field is divergence free, it will remain divergence free at subsequent time steps. The initial magnetic field is a divergence-free background magnetic field, a dipole magnetic field in the present study.

### 2.6. Boundary Conditions

At the bottom boundary ( $r = 90$  km), transport effects are assumed negligibly small. Therefore, the ion and neutral number densities are calculated by production and loss processes

$$\frac{\partial \bar{\rho}_s}{\partial t} = \sum_{t \neq s}^{l,m,e} (\bar{P}_{st} \bar{m}_t - \bar{L}_{st} \bar{\rho}_s) \quad (52)$$

The horizontal velocity components, i.e., the azimuthal (counterclockwise viewing from the Sun) component  $v_{s,\theta}$ , and z component  $v_{s,z}$ , are set to zero at the lower boundary. The boundary condition for the radial velocity component,  $v_{s,r}$ , is  $\partial v_{s,r} / \partial r = 0$ . At the lower boundary the temperatures are simply kept at their initial values, which are calculated by using empirical ionosphere model IRI2011 [Bilitza *et al.*, 2011] and empirical thermospheric model NRLMSISE00 [Picone *et al.*, 2002]. The simulations have shown that the lower boundary conditions for densities, velocities, and temperatures do not significantly affect the simulation results. This is because strong collisions make ions and neutral at the bottom barely respond to driving forces from the top boundary. Either  $\delta \mathbf{B} = 0$  or  $\mathbf{J} = \nabla \times \delta \mathbf{B} / \mu_0 = 0$  may be reasonable lower boundary conditions for the perturbation magnetic field since the bottom of the ionosphere may be regarded as the interface between the conducting ionosphere and the essentially nonconducting atmosphere (although not a perfect insulator). Both boundary conditions have been tested. While the detailed values are different for the two, the basic features of interest are retained in the simulation with either one. Results for the simulation with the boundary condition  $\mathbf{J} = 0$  at 90 km are presented.

The top boundary condition is a more interesting issue as it both serves as the driving source at high latitudes and may produce rereflection of the reflection from inside or lower boundary of the ionosphere. Ideally, the top boundary should be located at the magnetopause or in the solar wind and driven directly by the solar wind, in particular, when our model is extended to global three dimension. However, because in this study, we are testing the concept, our simulation domain has to be limited, up to only the topside ionosphere, so that somewhat artificial or numerical boundary conditions have to be used. At the top boundary (the altitude of the top boundary is flexible, several heights have been tested and 2000 km is used in this study), we impose open boundary condition for  $v_{s,r}$ ,  $n_s$ ,  $\delta B_r$  and  $\delta B_z$  (i.e., the spatial derivative of these variables with respect to  $r$  is zero), besides the imposed convection velocity  $v_{s,z}$  for the ion species at polar latitudes (see Figure 2). The boundary conditions for the azimuthal velocity and perturbation magnetic field are that  $v_{s,\theta,ij+1/2} = v_{s,\theta,ij-1/2}$  and  $\delta B_{\theta,ij+1/2} = \delta B_{\theta,ij-1/2}$  in accordance with the divergence-free magnetic field at the boundary.

### 2.7. Simulation Setup

The simulation can be either a fresh start run or a continuous run from a previous simulation. In the case of a fresh start, the simulation started from initial conditions with the densities of the ions ( $O^+$ ,  $H^+$ ,  $O_2^+$ ,  $N_2^+$ , and  $NO^+$ ) and neutrals ( $O$ ,  $H$ ,  $O_2$ ,  $N_2$ , and  $N$ ) provided by the International Reference Ionosphere (IRI2011) [Bilitza *et al.*, 2011] and the empirical thermospheric model NRLMSISE00 [Picone *et al.*, 2002], respectively. The three components of the ion and neutral velocities ( $v_{s,r}$ ,  $v_{s,\theta}$ , and  $v_{s,z}$ ) for all species are initially set to zero so do the three components of the perturbation magnetic field ( $\delta B_r$ ,  $\delta B_\theta$ , and  $\delta B_z$ ). The background magnetic field  $\mathbf{B}_0$  is a simple centered, tilted (dipole axis is shifted relative to the Earth's rotation axis) dipole field within the meridian plane.

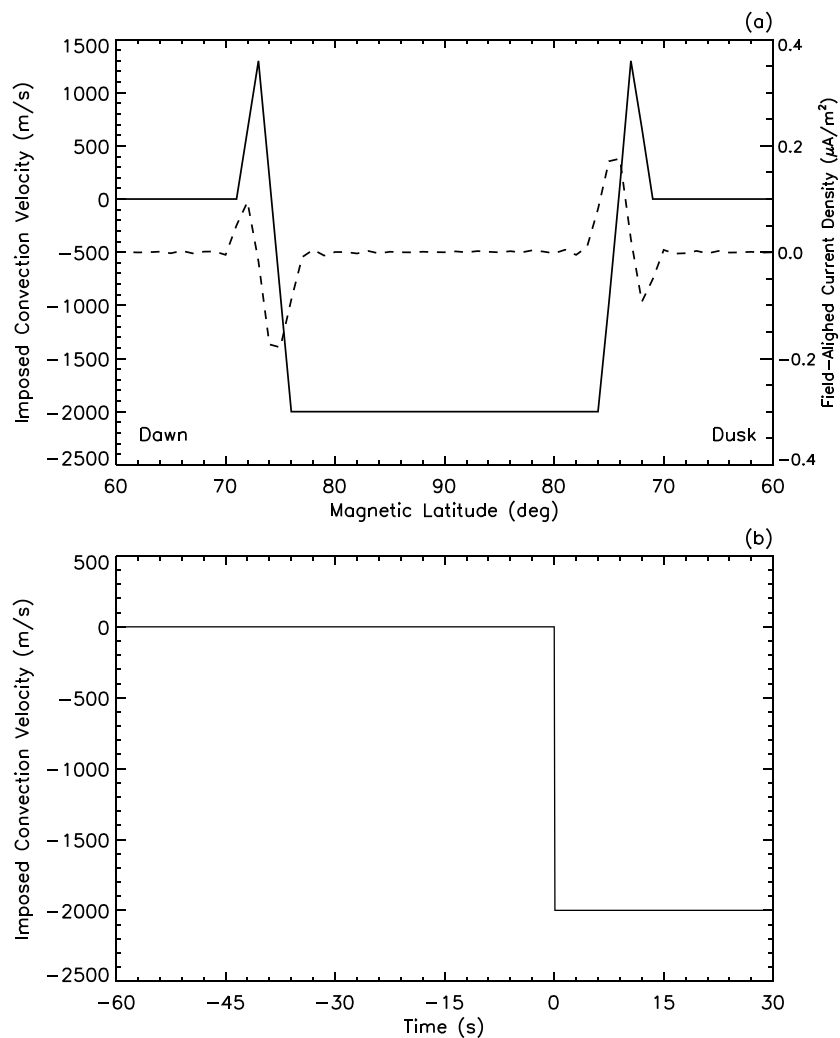


**Figure 2.** (a) Latitudinal distribution of the imposed convection velocity (positive sunward, solid line) and equivalent field-aligned current (FAC) density (positive upward, dashed line) at the top boundary for the Northern Hemisphere. (b) Time variation of the convection velocity imposed at the top boundary in the polar cap. Negative values are antisunward.

The 2-D simulation domain covers 90–2000 km in altitude and is divided into  $N_1 \times N_2$  cells with  $N_1 + 1$  grids radially and  $N_2 + 1$  grids azimuthally. In the present study we choose  $N_1 = 70$  and  $N_2 = 360$ . The radial grids are nonuniform with finer grids at lower altitudes and coarser grids at the higher altitudes. The radial distance of the grids changes from  $\Delta r \approx 5$  km in the  $E$  layer of the ionosphere to about 95 km at the top boundary (2000 km). The azimuthal grids are uniform, giving a constant grid size  $\Delta\theta = 1^\circ$ .

The model was run for the first 1 min without explicitly specifying the driving forces from the magnetosphere at the top boundary (altitude  $z = 2000$  km). Then at the top boundary an out of meridian velocity component for all ion species is imposed. The imposed velocity is assumed to be antisunward ( $v_{s,z} < 0$ ) in the region over latitudes of  $75^\circ$  (polar cap) and sunward between  $74^\circ$  and  $72^\circ$  to mimic the magnetospheric return flow. The velocity reversal occurs at latitudes between  $74^\circ$  and  $75^\circ$ . Below  $72^\circ$  the imposed velocity is set to zero. The imposed velocity in the polar cap reaches  $-2000$  m/s after 0.1 s ramp time and keeps at that value thereafter as shown in Figure 2b. The time at which the convection velocity starts imposing at the top boundary is referenced as  $t = 0$  hereafter. Note that in collisionless or weakly collisional MHD, flow reversals due to two-cell convection are equivalent to a pair of field-aligned (region 1) currents (FACs) from  $\sim 72.5^\circ$  to  $\sim 77^\circ$  in the present simulation, because the corresponding magnetic perturbations are proportional to the plasma velocity as described by the Walén relation. A pair of region 2 currents appears where the flow goes back to zero at lower latitudes. Figure 2a shows the magnetic latitude distribution of the velocity and equivalent FACs

imposed at the top boundary after the imposed velocity reaches its maximum magnitude. We also emphasize that the FACs are not imposed at the top boundary but self-consistently calculated from the imposed convection velocity, which drives the magnetic field perturbations. Furthermore, the propagation of the FACs into the simulation domain is governed by the collisional-Hall MHD.

### 3. Results

In our previous studies [Song *et al.*, 2009; Tu *et al.*, 2011, 2014] we have applied inductive-dynamic approach to the variation of ionospheric perturbations in one-dimensional geometry. These simulations have illustrated that the dynamic M-I coupling is through MHD waves instead of electrostatic electrical fields or field-aligned currents. Nevertheless, the 1-D simulations cannot provide global views of the M-IT coupling due to the restriction that the spatial variations of all the variables are only along the altitude, and more importantly, field-aligned currents are not included from the solutions. In the present study a 2-D multi-fluid inductive-dynamic simulation provides a global picture of the M-I coupling through the Alfvén waves and show the dynamic evolution of the field-aligned currents and formation of the Pedersen currents. Note that the multiple ion and neutral species are necessary for self-consistently calculating the time-dependent photochemistry while the multifluid is required to appropriately account for the transport of individual ion and species.

#### 3.1. Two-Dimensional Overview of Dynamic M-I Coupling

We first present a global overview (although limited to two dimensions, in a dawn-dusk magnetic meridian) by showing the propagation of the magnetic and velocity perturbations in response to an imposed antisunward convection velocity in the polar cap at the top boundary of the simulation domain. Figures 3 and 4 display distributions of Sun-Earth line components of the ion bulk velocity  $v_z = \sum_s n_s v_{s,z} / n_e$ , where the summation runs over all the ion species and perturbation magnetic field  $\delta B_z$  as functions of magnetic latitude and height at selected times. The time is in units of the Alfvén travel time, which is the time for the Alfvén wave to propagate from the top to the bottom boundary, using the local ion mass density and magnetic field along the magnetic field threading the north pole. As discussed by Tu *et al.* [2014], based on simulations using different heights of the top boundary, the Alfvén time is the characteristic time scale describing the dynamic processes of M-IT coupling. The actual wave propagation time is slightly longer because of the neutral inertial loading in the low-altitude ionosphere, particularly the E region [Song *et al.*, 2005].

Although the simulation covers the whole 360° of meridian plane, the Southern and Northern Hemispheres are characteristically similar with differences mostly due to the differences in the parameters from the empirical models. Note in the short time period considered, the initial ionosphere/thermosphere parameters have not changed appreciably from those specified by the empirical models. The background magnetic fields are opposite in the two hemispheres. In the following we discuss mostly the results from one hemisphere.

Several features can be easily seen from these figures.

1. It is obvious that perturbations in the ion velocities and magnetic field propagate downward along the magnetic field lines at latitudes above 72°. The propagation speed of the perturbations is near the local Alfvén speed as confirmed by calculating the integrated time for the perturbation front to propagate from the top to a given altitude. Corresponding to the antisunward convection velocity imposed at the top boundary, the velocity perturbations in the polar cap of both hemispheres are antisunward but sunward in the subauroral region at lower latitude than the reversal at about 74.5°. The perturbation magnetic field in the Northern Hemisphere, on the other hand, is in the opposite directions to that in the Southern Hemisphere as expected from the Walén relation for parallel propagation.
2. The velocity decreases in magnitude while propagating downward, but the magnitude of the perturbation magnetic field remains nearly constant. To understand this feature, it is instructive to understand processes associated with a single-incident Alfvén wave into the ionosphere from the magnetosphere. Above the F-2 plasma density peak, the Alfvén speed decreases as propagating downward. Although the Alfvén speed increases below the density peak, the propagation speed continues to decrease because of the inertia-loading process due to heavier collisions [Song *et al.*, 2005]. Because of the collisions in the ionosphere, the wave energy flux is continuously damped. Because of the plasma density above F-2 peak increases with the decreasing height, which changes continuously the index of refraction of the medium, the wave experiences continuous reflection and penetration. The magnetic perturbation of the reflected wave reverses direction from the incident one. The resulting velocity and magnetic perturbations are a

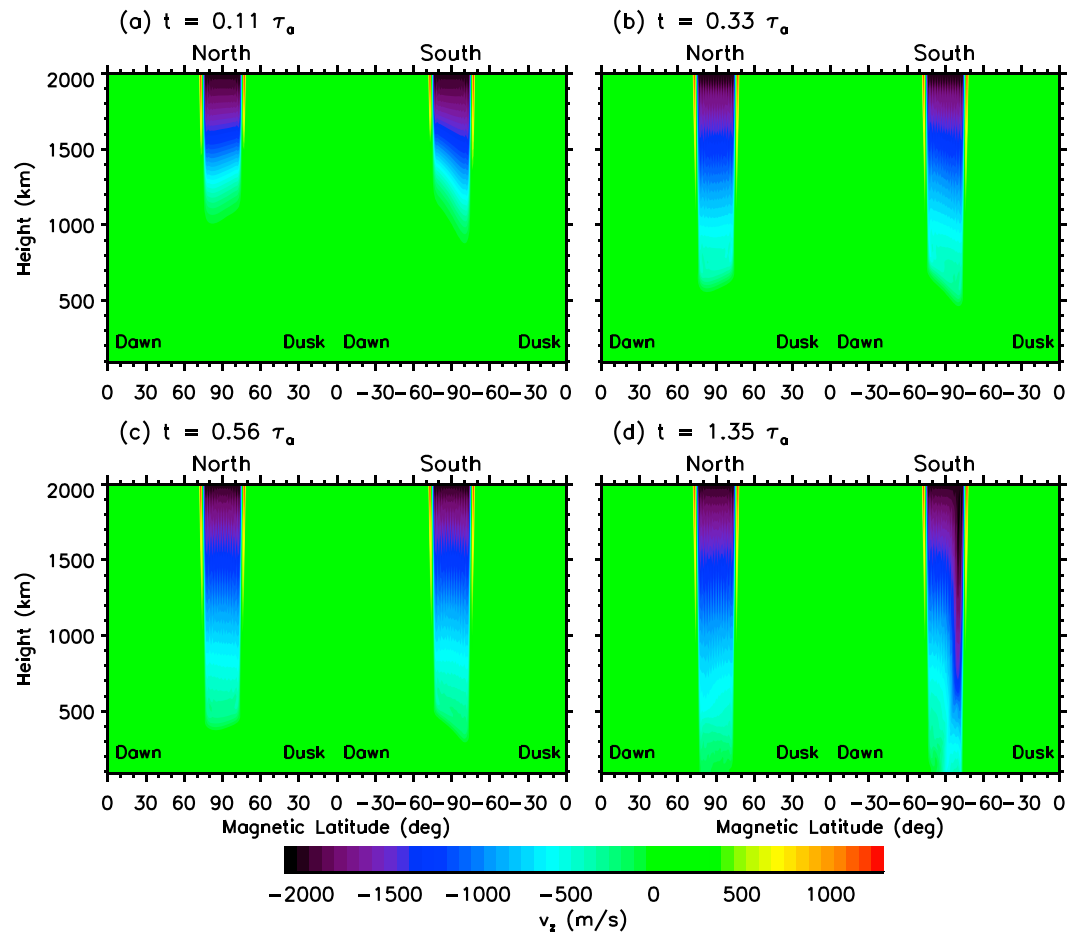


**Figure 3.** (a–d) Distribution of Sun–Earth line component of the ion bulk velocity  $v_z = \sum_s n_s v_{s,z} / n_e$  as a function of magnetic latitude and altitude at selected times. Positive values are sunward.  $\tau_a = 0.88$  s is the Alfvén travel time, the time for the Alfvén wave to propagate from the top boundary (2000 km) to the bottom boundary (90 km) along the field line threading the north dipole pole. In each panel, the distributions of  $v_z$  in both Northern and Southern Hemispheres are displayed.

combination of propagation slowdown, absorption, and reflection. Further complicating the situation is that the reflected wave may be rereflected. When absorption and reflection is not considered, the energy flux reservation leads to variation of the velocity (perturbation magnetic field) magnitude proportional to  $\rho^{-1/4}$  ( $\rho^{1/4}$ ) [e.g., Song and Vasyliūnas, 2014]. Meanwhile, the continuous reflection throughout the wave propagation path results in that the velocity (perturbation magnetic field) at any given altitude is the superposition of the incident wave, locally reflected wave, and wave reflected from a lower altitude but at an earlier time, as well as the reflected wave being reflected from higher altitude [Tu and Song, 2013]. In the low-altitude ionosphere, particularly in the E region, the ion collisions cause the significant dissipation of the wave energy, making the situation even more complicated. In the present simulation the plasma density is lower on the duskside of the Southern Hemisphere which results in a higher Alfvén speed. The front in this region reaches the lower boundary earlier than that on the dawnside. Therefore, the perturbation seen on the duskside is accumulated from the perturbation at the top boundary over a longer time. In addition, from the Walén relation, the greater Alfvén speed leads to a greater velocity perturbation. This is why the perturbations seen on the duskside of the southern polar cap are the strongest.

3. The velocity perturbation at low altitudes may be strong with the amplitude comparable to or even larger than that imposed at the top boundary. Such strong velocity perturbations are seen in the southern polar cap around  $-80^\circ$  latitude below about 300 km as evident in Figure 3d and is more clearly shown in Figure 5, which is a plot of altitude variation of  $v_z$  at several chosen times. The wave front reaches the bottom of the ionosphere at  $t \sim 1\tau_a$  (about 0.88 s). After that time the velocity may be overshoot, as shown by, for example, the velocity profile at  $t = 4.18\tau_a$ . Since the heating rates dependent on the square of the velocity

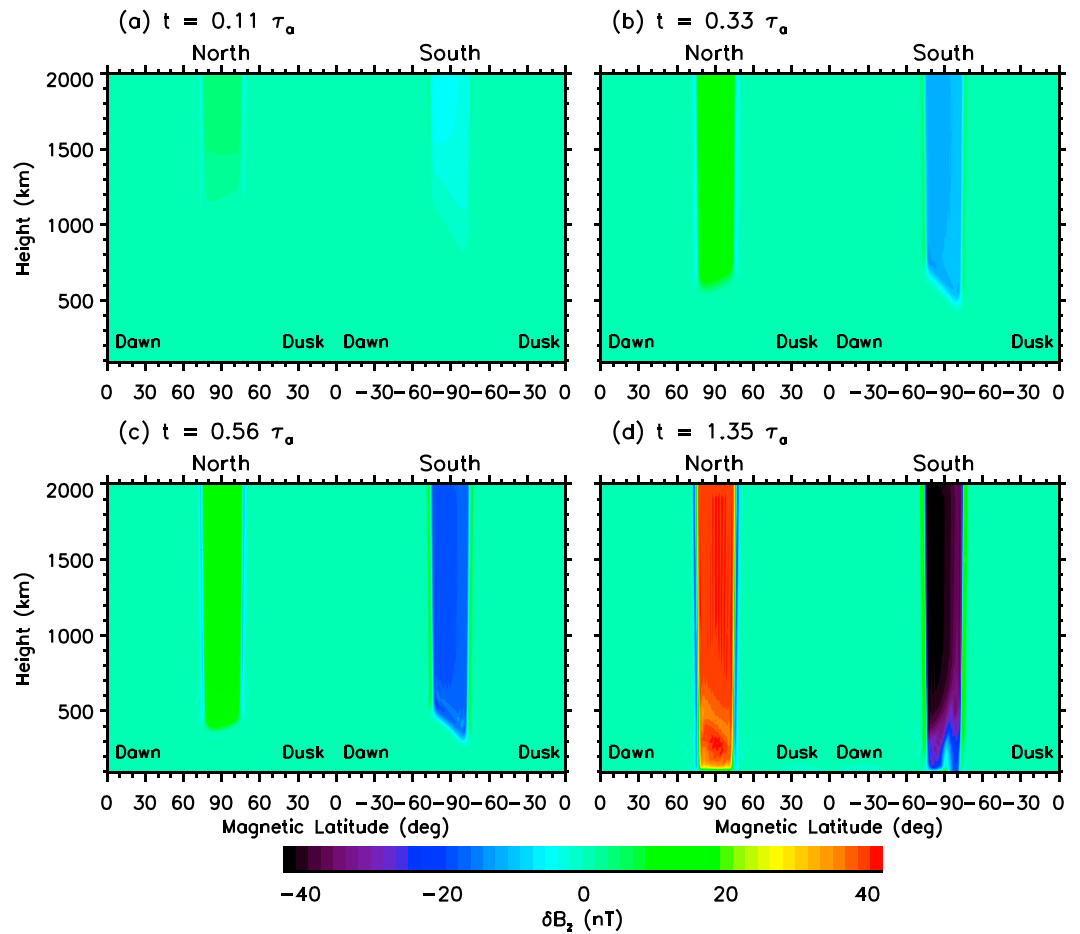


**Figure 4.** The same format as that of Figure 3 but for the Sun-Earth line component of the perturbation magnetic field  $\delta B_z$ . Positive values are sunward.

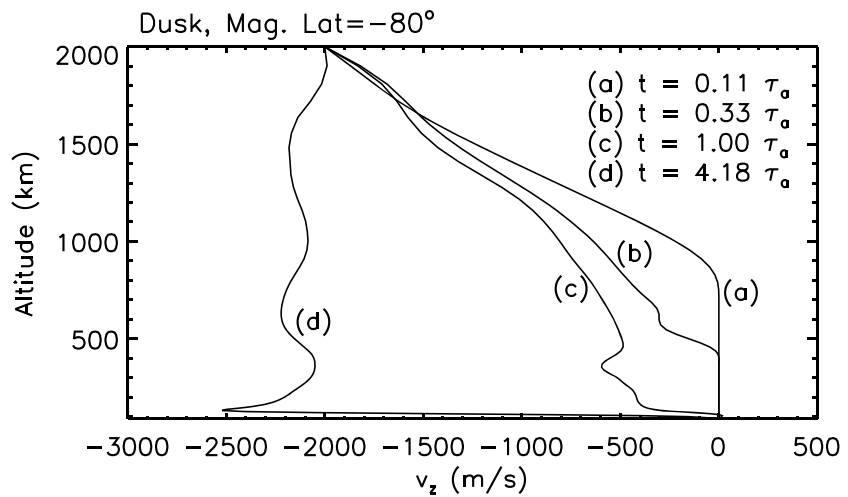


**Figure 5.** Altitude profiles of antisunward component,  $v_z$ , of the ion bulk velocity at magnetic latitude  $-80^\circ$  at times (a)  $0.11 \tau_a$ , (b)  $0.33 \tau_a$ , (c)  $1.00 \tau_a$ , and (d)  $4.18 \tau_a$ .

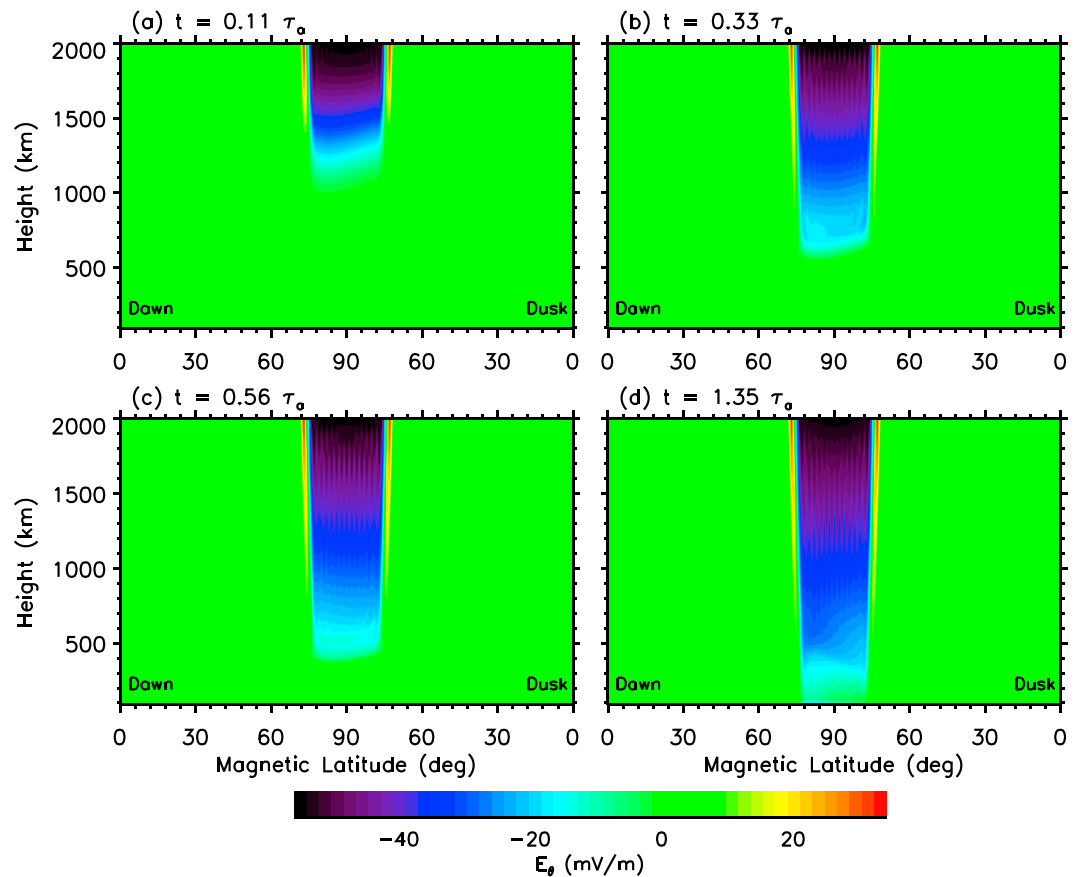


**Figure 6.** (a–d) Distribution of dawn-dusk electric field as a function of magnetic latitude and altitude for the Northern Hemisphere at selected times. Negative values are duskward.

difference between the plasma and neutrals, or essentially the plasma velocity before the neutrals have been accelerated significantly, the strongest heating will be concentrated in the regions of the plasma velocity overshooting. This issue, as well as thermosphere heating, will be further discussed in a future publication.

It is also interesting to examine the distribution and variation of dawn-dusk electric field. Figure 6 shows the dawn-dusk electric field as the function of latitude and height for the Northern Hemisphere at several selected times. The electric field is directed from dawn to dusk in the polar cap where the velocity perturbations are antisunward and is from dusk to dawn at lower altitudes where the velocity perturbations are sunward, consistent with the direction of  $-\mathbf{v} \times \mathbf{B}$ , implying that the first term of (4) is dominant. It is clear that the electric field is associated with the Alfvén waves, propagating downward with the Alfvén speed. In addition, the same as the velocity and magnetic perturbations, the electric field is altitude dependent; in general, its magnitude decreases with decreasing height, indicating that the M-I coupling is not by electric field mapping along the magnetic field lines until the steady state is reached. Of course this is by no means to say that the M-I coupling using the electric field mapping, as commonly employed in the current sophisticated 3-D M-I coupling models, is completely invalid. The present study, however, indicates that one needs to keep in mind the disadvantage of the electric field mapping; i.e., it cannot be used to investigate the coupling processes during the dynamic stages when the ionosphere/thermosphere transits from one quasi steady state to another.

It is seen from Figure 5 that the perturbation magnetic field enhances at all altitudes due to the superposition of the incident and reflected waves. Then the velocity and electric field should reduce at all altitudes. Instead, as seen from Figures 4 and 6 the reduction of the velocity and electric field is limited at low altitudes (primarily below 1000 km). As we have discussed before, in general, the signal is a summation of the incidence and reflection. Whether the two enhance or cancel each other depends on the phase between the two.

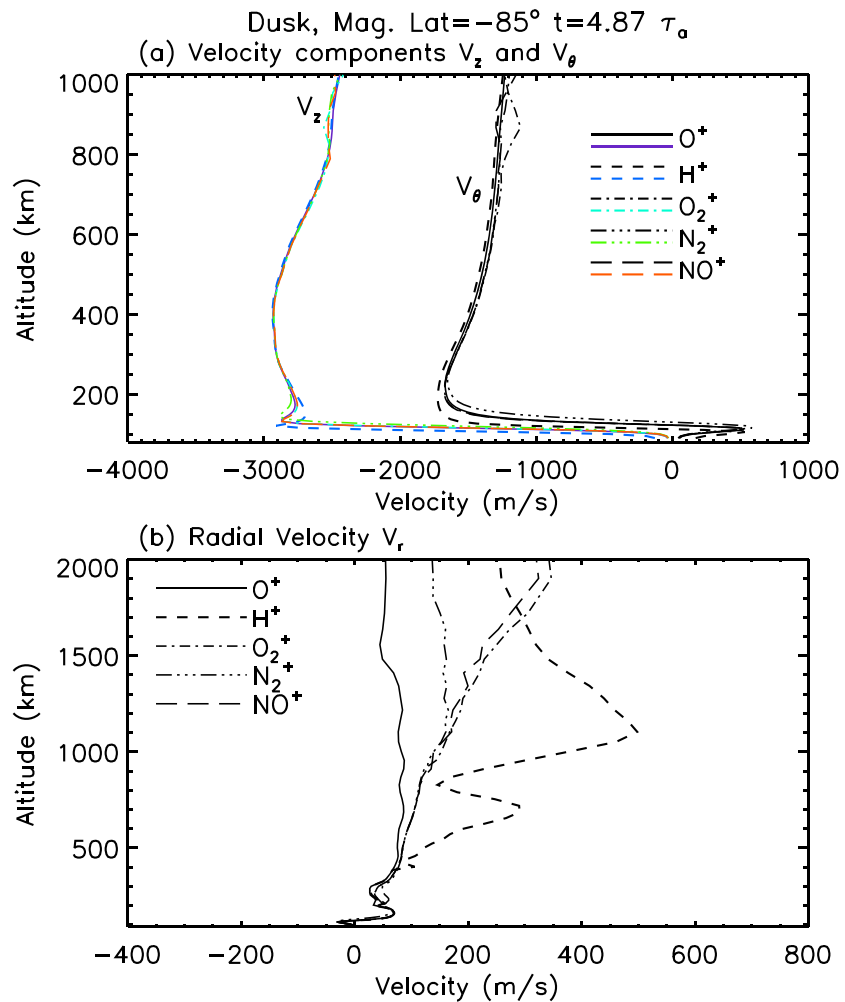


**Figure 7.** (a) Altitude variations of horizontal velocity components  $v_z$  (negative antisunward) and  $v_\theta$  (negative duskward) of  $O^+$ ,  $H^+$ ,  $O_2^+$ ,  $N_2^+$ , and  $NO^+$ , and (b) radial velocity of these ion species at magnetic latitude  $-85^\circ$  and 4.87 Alfvén travel times.

The phase between the two depends on the property of the source. For example, if the source is periodical oscillation, we should see periodical resultant signals. If the source is a step function, which is what we refer to as “sustained perturbation” and can be decomposed into sinusoidal oscillations with no phase shift only at one instance. As the oscillations propagate, different frequencies, mostly because of different wavelengths, reflect differently at different altitudes. Our simulation at the current stage has a vertical scale of 1920 km. This effectively limits the wavelength. The dominant wavelength, however, is determined by the scale of the ionospheric layer. As shown by *Song and Vasyliūnas* [2014], in the location just above the reflection, the magnetic field tends to enhance and the velocity tends to cancel. The vertical extent of this enhancement and cancellation is limited by the wavelength of the perturbation. The actual velocity perturbation is also dependent on the Alfvén speed as we explained above. Therefore, the difference between the field perturbation enhancement and reduction of the velocity perturbation is, in general, understandable. Specifically, its vertical scale is determined by the vertical scale of the ionosphere. The electric field perturbation is roughly proportional to the velocity perturbation.

Since the present simulation model includes dynamics of multiple ion species, we can also examine the behavior of different ion species in the process of the Alfvén wave propagation and reflection. Figure 7 shows altitude distribution of three velocity components of  $O^+$ ,  $H^+$ ,  $O_2^+$ ,  $N_2^+$ , and  $NO^+$  ions at  $-85^\circ$  on the duskside, and at  $t = 4.87 \tau_a$ . It is interesting to note that the horizontal ( $z$  and  $\theta$ ) velocity components of all the ion species are nearly the same, indicating the combined effects of Lorentz force, pressure gradient, advection, and collisions are almost the same for different ion species. The radial velocities, however, can be quite different owing

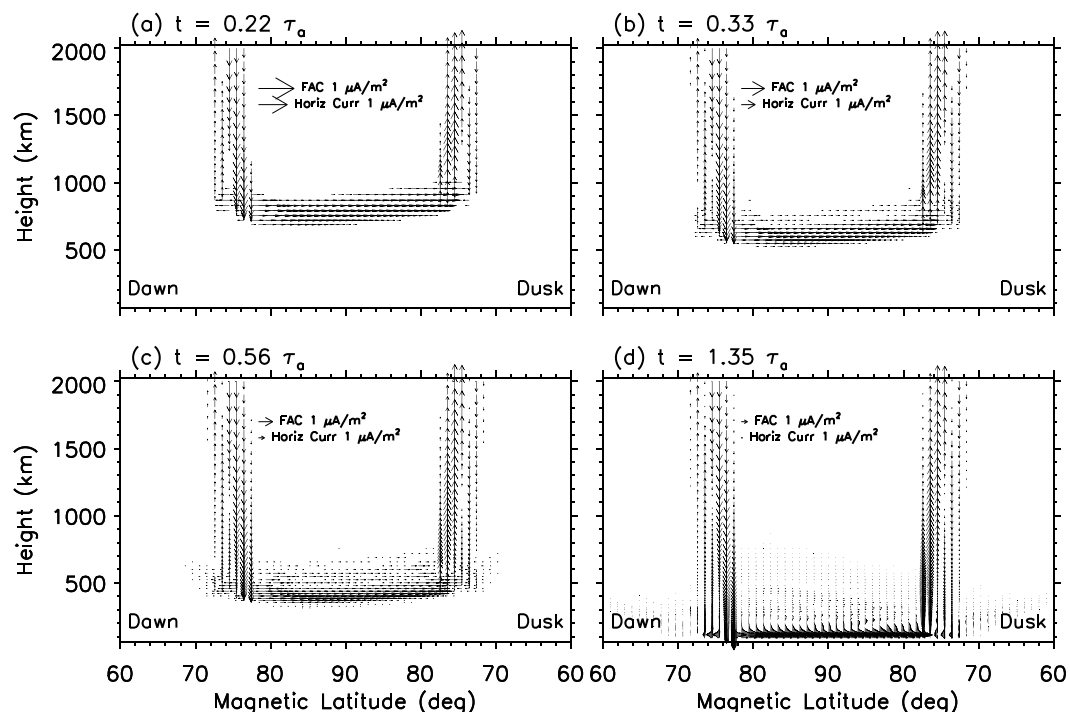


**Figure 8.** (a–d) Distribution of field-aligned currents (FAC) and horizontal closure currents for Northern Hemisphere at four given times.

to the different masses of these ion species and radial component of the pressure gradient subtracted by the gravity.

An interesting feature, which has been discussed in our previous study [Tu *et al.*, 2014], is that  $v_\theta$ , as well as  $\delta B_\theta$  (data not shown), is produced even though the ionosphere is pushed at the top boundary only in the anti-sunward direction (i.e., only  $v_z$  is imposed at the top boundary). This is essentially a result of the dynamic Hall effect. However, different from the conventional Hall effect which is based on the Hall and Pedersen conductivities and produces  $v_\theta$  only in regions where the collision frequencies are high, the Hall effect in the present inductive-dynamic simulation results from the  $\theta$  component of  $\mathbf{J} \times \mathbf{B}$  force so that  $v_\theta$  and also  $\delta B_\theta$  manifest not only in the low-altitude ionosphere where the collisions are strong but also at high altitudes where the collisions are weak (so that the conductivities are negligibly small). In other words, the dynamic Hall effect is an intrinsic aspect, with or without the collisions, of the M-I coupling [Tu *et al.*, 2014].

### 3.2. Dynamics of Field-Aligned and Horizontal Closure Currents

The above section shows that the Alfvén waves propagating downward carry energy and momentum from the magnetosphere to the ionosphere/thermosphere, which drives ionospheric motion. It is apparent that the M-IT coupling is through the Alfvén waves. Associated with the Alfvén waves, if the driver in the magnetosphere is not uniform, field-aligned currents are produced and propagate downward with the Alfvén waves and the gradients of the field-aligned currents are closed locally by currents flowing perpendicular to the magnetic field (basically horizontal at polar latitudes). Figure 8 displays field-aligned currents and their closure currents with vectors for the northern high-latitude region at four given times. From the figure we see that on both dawnside and duskside, a pair of field-aligned current sheets is produced and propagate downward at the same speed as the velocity and magnetic field perturbations. On the dawnside the region 1 current flows downward (above about  $74^\circ$ ) and region 2 upward, respectively, while the regions 1 and 2 currents on the duskside have a reversed polarity. Such a pattern of the simulated FACs is consistent with the sense of regions 1 and 2 field-aligned current sheets typically observed for the two-cell convection pattern at polar latitudes [Iijima and Potemra, 1976].

Specifically, accompanying the Alfvén wave front, there are currents perpendicular to the field lines that close the FACs, partially flowing from dawn to dusk between two region 1 field-aligned current sheets at higher latitudes (at latitudes above  $\sim 77^\circ$ ), and flowing from dusk and dawn between the regions 1 and 2 FACs on both

dawnside and duskside. Note that since the closure currents are associated with the gradient of the FACs, they are strongest at the Alfvén wave front and weak after the passage of the front, as shown in Figure 8d. As the wave front goes down, the density increases and the wavelength decreases, and thus the current magnitude increases. Note that the plasma density decreases below the F-2 peak height, but the neutral density increases. Due to the inertial loading effects through frequent ion-neutral collisions, the wavelength decreases even below the F-2 peak height. When the wave front reaches the bottom of the ionosphere, the horizontal closure currents are concentrated around about 110 km, forming the so-called Pedersen currents. There are also Hall currents (data not shown) but much weaker than the field-aligned and horizontal closure currents. We should point out that the Pedersen current is related to collisions. Above 250 km, collisions are weak and the horizontal closure currents are associated with the propagation of the Alfvén waves. In a later time as the Alfvén waves propagate and reflect, the conventional Pedersen and Hall (not shown) currents are the steady state closure currents of the FACs. Our simulation captures the dynamical evolution of the FACs and development of the Pedersen currents.

It is also noted that inside the polar cap between the two region 1 current sheets there are perpendicular closure currents above the Pedersen current, which are carried by the reflected Alfvén wave front, just like the incident wave front carries the perpendicular currents. There are also quite weak but observable perpendicular (essentially azimuthal) currents extended outside the polar cap (below the latitudes of the region 2 current sheets on both dawnside and duskside). This extension of the perpendicular currents is caused by the non-ideal MHD effect, associated with primarily the term  $\nabla n_e \times \nabla T_e / en_e$  in the magnetic induction equation (8) which causes magnetic field perturbation in Sun-Earth direction ( $\delta B_z$  component) in the 2-D geometry. This magnetic field perturbation in turn produces a azimuthal current  $\mu_0 J_\theta = -\partial \delta B_z / \partial r$ . This current is very weak but may become observable in the low-altitude ionosphere where the electron density is very low since it is roughly proportional to the inverse of the electron density. At the lowest altitude, the electron density and temperature may be negligibly small, this azimuthal current may be too weak to be visible.

#### 4. Summary and Discussion

In the present study we have used a newly developed global 2-D inductive-dynamic numerical model of ionosphere-thermosphere to examine the dynamic processes of the magnetosphere-ionosphere coupling. In this model the time-dependent continuity, momentum, and energy equations of the electron and multiple ion and neutral species with photochemistry, plus Maxwell's equations (Faraday's and Ampere's laws) are self-consistently solved in a 2-D global ionospheric geometry. With such an inductive-dynamic approach, not only sound wave modes but also all the possible MHD wave modes are retained in the solutions of the governing equations. This allows us to self-consistently evaluate the dynamic responses of the ionosphere/thermosphere to the magnetosphere disturbances (here the imposed convection velocity). The governing equations solved in the model are a set of multifluid-collisional-Hall MHD equations which are one of the unique features of our ionosphere/thermosphere model. The simulation results presented here further illustrate that the M-I coupling is via Alfvén waves. The results also demonstrate propagation and evolution of the field-aligned currents and the dynamic formation of the cross-polar cap electric field, and ionospheric Pedersen currents.

The evolution of the field-aligned currents and accompanying horizontal closure currents perpendicular to the magnetic field lines, to our knowledge, is for the first time simulated self-consistently. It is clearly shown that the FACs are carried by the Alfvén waves. The closure currents are formed at the propagating front of the FACs, even in the high altitudes (above 250 km) where the collisions are essentially absent. Therefore, the closure currents are not associated with the Pedersen conductivity which are related to the ion-neutral and electron-neutral collisions. Instead, the closure currents are associated with the Alfvén wave front. As shown in Figure 6 the electric field propagates with the Alfvén speed so that the electric field is also the consequence of the Alfvén wave propagation, reflection, and rereflection. In conclusion, the M-I coupling is not established by the field-aligned currents nor by the mapped magnetospheric electric field.

One of consequences of M-I coupling through Alfvén waves is the enhancement of the ion velocity through wave reflection and rereflection. Such increased ion velocity causes enhanced ionosphere/thermosphere frictional heating and thus the increase of the ion and neutral temperatures. We have not discussed simulation results related to the physical processes of heating and temperature variations, because the focus of the paper

is to describe the simulation model and test the code through the discussion of the simulation results in accordance with our previous 1-D simulation results on the M-I coupling. We will discuss these processes in a future publication.

#### Acknowledgments

This study was supported by the NSF grants AGS-1559717 and AGS-1248242, and NASA grant NNX12AD22G to the University of Massachusetts Lowell. J. Tu thanks Jed Brown, Barry Smith, and Dmitry Karpeev at Mathematics and Computer Science Division of Argonne National Laboratory for their valuable help to using the PETSc software package. We thank V. M. Vasyliūnas for helpful comments and suggestions. The simulation code and simulation data in compressed ASCII format are available from the authors upon request.

#### References

- Balay, S., W. D. Gropp, L. C. McInnes, and B. F. Smith (1997), Efficient management of parallelism in object oriented numerical software libraries, in *Modern Software Tools in Scientific Computing*, edited by S. Balay et al., pp. 163–202, Birkhäuser Press, Cambridge, Mass.
- Banks, P. M., and G. Kockarts (1973), *Aeronomy: Part B*, 355 pp., Acad. Press, San Diego, California.
- Bates, D. R. (1951), The temperature of the upper atmosphere, *Proc. Phys. Soc. B*, *64*, 805–821.
- Billitz, D., L. A. McKinnell, B. W. Reinisch, and T. Fuller-Rowell (2011), The international reference ionosphere (IRI) today and in the future, *J. Geodesy*, *85*, 909–920, doi:10.1007/s00190-010-0427-x.
- Birk, G. T., and A. Otto (1996), A three-dimensional plasma-neutral gas-fluid code, *J. Comp. Phys.*, *125*, 513–525.
- Chapman, S., and T. G. Cowling (1970), *The Mathematical Theory of Nonuniform Gases*, Cambridge Univ. Press, New York.
- Colegrove, F. D. (1966), Atmospheric composition in the lower thermosphere, *J. Geophys. Res.*, *71*, 2227–2236.
- Curtiss, C. F., and J. O. Hirschfelder (1952), Integration of stiff equations, *Proc. Nat. Acad. Sci.*, *38*(3), 235–243.
- Dickinson, R. E., and E. C. Ridley (1972), Numerical solution for the composition of a thermosphere in the presence of a steady subsolar-to-antisolar circulation with application to Venus, *J. Atmos. Sci.*, *29*, 1557–1570.
- Harris, I., and W. Priester (1962), Time-dependent structure of the upper atmosphere, *J. Atmos. Sci.*, *19*, 286–301.
- Hirt, C. W. (1968), Heuristic stability theory for finite-difference equations, *J. Comp. Phys.*, *2*, 339–355.
- Huang, C. Y., Y.-J. Su, E. K. Sutton, D. R. Weimer, and R. L. Davidson (2014), Energy coupling during the August 2011 magnetic storm, *J. Geophys. Res. Space Physics*, *119*, 1219–1232, doi:10.1002/2013JA019297.
- Huba, J. D., G. Joyce, and J. A. Fedder (2000), Sami2 is another model of the ionosphere (SAM2): A new low-latitude ionosphere model, *J. Geophys. Res.*, *105*, 23,035–23,053.
- Hughes, W. J. (1974), The effect of the atmosphere and ionosphere on long period magnetospheric micropulsations, *Planet. Space Sci.*, *22*, 1157–1172.
- Iijima, T., and T. A. Potemra (1976), The amplitude distribution of field-aligned currents at northern high latitudes observed by Triad, *J. Geophys. Res.*, *81*, 2165–2174.
- Kelley, M. C. (2009), *The Earth's Ionosphere, Plasma Physics and Electrodynamics*, 2nd edn, 576 pp., Acad. Press, Burlington, Mass.
- Kelley, C. T. (2003), *Solving Nonlinear Equations with Newton's Method*, 104 pp., SIAM, Philadelphia, Pa.
- Kockarts, G., and W. Peetermans (1970), Atomic oxygen infrared emission in the Earth's upper atmosphere, *Planet. Space Sci.*, *18*, 271–285.
- Kockarts, G. (1980), Nitric oxide cooling in the terrestrial thermosphere, *Geophys. Res. Lett.*, *7*(2), 137–140.
- Lysak, R. L. (2004), Magnetosphere-ionosphere coupling by Alfvén waves at midlatitudes, *J. Geophys. Res.*, *109*, A07201, doi:10.1029/2004JA010454.
- Lysak, R. L., and C. Dum (1983), Dynamics of magnetosphere-ionosphere coupling including turbulent transport, *J. Geophys. Res.*, *88*, 365–380.
- Lysak, R. L., C. L. Waters, and M. D. Sciffer (2013), Modeling of the ionospheric Alfvén resonator in dipolar geometry, *J. Geophys. Res. Space Physics*, *118*, 1514–1528, doi:10.1002/jgra.50090.
- Millward, G. H., R. J. Moffett, W. Quegan, and T. J. Fuller-Rowell (1996), A coupled thermospheric-ionospheric-plasmasphere model (CTIP), in *STEP: Handbook of Ionospheric Models*, edited by R. W. Schunk and J. H. Allen, pp. 239–279, Utah State Univ., Logan, Utah.
- Mitra, A. P. (1968), A review of D-region process in non-polar latitudes, *J. Atmos. Terr. Phys.*, *30*, 1065–1114.
- Otto, A., D. Lummerzheim, H. Zhu, O. Lie-Svendsen, M. H. Rees, and B. S. Lanchester (2003), Excitation of tall auroral rays by ohmic heating in field-aligned current filaments at F region heights, *J. Geophys. Res.*, *108*, 8017, doi:10.1029/2002JA009423.
- Parker, E. N. (2007), *Conversations on Electric and Magnetic Fields in the Cosmos*, 178 pp., Princeton Univ. Press, Princeton, N. J.
- Picone, J. M., A. E. Hedin, D. Drob, and A. Aikin (2002), NRL-MSISE-00 empirical model of the atmosphere: Statistical comparisons and scientific issues, *J. Geophys. Res.*, *107*, 1468, doi:10.1029/2002JA009430.
- Richards, P., J. Fennelly, and D. Torr (1994), EUVAC: A solar EUV flux model for aeronomic calculations, *J. Geophys. Res.*, *99*, 8981–8992.
- Richmond, A. D. (1995), Ionospheric electrodynamics, in *Handbook of Atmospheric Electrodynamics*, vol. II, edited by H. Volland, pp. 249–290, CRC Press, Boca Raton, Fla.
- Stolarski, R. S., P. B. Hays, and R. G. Roble (1975), Atmospheric heating by solar EUV radiation, *J. Geophys. Res.*, *80*, 2266–2276.
- Robel, R. G., E. C. Ridley, and R. E. Dickinson (1987), On the global mean structure of the thermosphere, *J. Geophys. Res.*, *92*, 8745–8758.
- Schunk, R. W., and A. F. Nagy (2000), *Ionospheres: Physics, Plasma Physics, and Chemistry*, 554 pp., Cambridge Univ. Press, New York.
- Sigmund, O., and J. Petersson (1998), Numerical instabilities in topology optimization: A survey on procedures dealing with checkerboards, mesh-dependencies and local minima, *Str. Opt.*, *16*, 68–75.
- Smith, F. L., and C. Smith (1972), Numerical evaluation of Chapman's grazing incidence integral  $ch(X, \chi)$ , *J. Geophys. Res.*, *77*, 3592–3597.
- Smithro, C. G., and S. C. Solomon (2008), An improved parameterization of thermal electron heating by photoelectrons, with application to an X17 flare, *J. Geophys. Res.*, *113*, A08307, doi:10.1029/2008JA013077.
- Solomon, S. C., P. B. Hays, and V. J. Abreu (1988), The auroral 6300 Å emission: Observations and modeling, *J. Geophys. Res.*, *93*(A9), 9867–9882.
- Song, P., V. M. Vasyliūnas, and L. Ma (2005), Solar wind-magnetosphere-ionosphere coupling: Neutral atmosphere effects on signal propagation, *J. Geophys. Res.*, *110*, A09309, doi:10.1029/2005JA011139.
- Song, P., V. M. Vasyliūnas, and X.-Z. Zhou (2009), Magnetosphere-ionosphere/thermosphere coupling: Self-consistent solutions for a one-dimensional stratified ionosphere in three-fluid theory, *J. Geophys. Res.*, *114*, A08213, doi:10.1029/JA013629.
- Song, P., and V. M. Vasyliūnas (2014), Effect of horizontally inhomogeneous heating on flow and magnetic field in the chromosphere of the Sun, *Astrophys. J. Letts.*, *796*(2), L23, doi:10.1088/2041-8205/796/2/L23.
- Streltsov, A. V., and W. Lotko (2008), Coupling between density structures, electromagnetic waves and ionospheric feedback in the auroral zone, *J. Geophys. Res.*, *113*, A05212, doi:10.1029/2007JA012594.
- Strobel, D. F., C. B. Opal, and R. R. Meier (1980), Photoionization rates in the night-time E- and F-region ionosphere, *Planet. Space Sci.*, *28*, 1027–1033.
- Swartz, W. E., and J. S. Nisbet (1972), Revised calculations of F region ambient electron heating by photoelectrons, *J. Geophys. Res.*, *77*(31), 6259–6261.

- Torr, M. R., P. G. Richards, and D. G. Torr (1980), The solar ultraviolet heating efficiency of the midlatitude thermosphere, *Geophys. Res. Lett.*, *7*(5), 373–376.
- Tu, J., and P. Song (2013), A study of Alfvén wave propagation and heating the chromosphere, *Astrophys. J.*, *777*, 53, doi:10.1088/0004-637X/777/1/53.
- Tu, J., P. Song, and V. M. Vasyliunas (2011), Ionosphere/thermosphere heating determined from dynamic magnetosphere-ionosphere/thermosphere coupling, *J. Geophys. Res.*, *116*, A09311, doi:10.1029/2011JA016620.
- Tu, J., P. Song, and V. M. Vasyliunas (2014), Inductive-dynamic magnetosphere-ionosphere coupling via MHD waves, *J. Geophys. Res.*, *119*, 530–547, doi:10.1002/2013JA018982.
- Vasyliunas, V. M., (1970), Mathematical models of magnetospheric convection and its coupling to the ionosphere, in *Particles and Fields in the Magnetosphere*, edited by B. McCormac, pp. 60–71, D. Reidel Publ. Co., Norwell, Mass.
- Vasyliunas, V. M. (2012), The physical basis of ionospheric electrodynamics, *Ann. Geophys.*, *30*, 357–369, doi:10.5194/angeo-30-357-2012.
- Vasyliunas, V. M., and P. Song (2005), Meaning of ionospheric Joule heating, *J. Geophys. Res.*, *110*, A02301, doi:10.1029/2004JA010615.
- Wolf, R. A. (1970), Effects of ionospheric conductivity on convective flow of plasma in the magnetosphere, *J. Geophys. Res.*, *75*(25), 4677–4698, doi:10.1029/JA075i025p04677.
- Woodroffe, J. R., and R. L. Lysak (2012), Ultra-low frequency wave coupling in the ionospheric Alfvén resonator: Characteristics and implications for the interpretation of ground magnetic fields, *J. Geophys. Res.*, *117*, A03223, doi:10.1029/2011JA017057.
- Zhu, H., A. Otto, D. Lummerzheim, M. H. Rees, and B. S. Lanchester (2001), Ionosphere-magnetosphere simulation of small-scale structure and dynamics, *J. Geophys. Res.*, *106*, 1795–1806.